Remote Sensing of Environment 305 (2024) 114075

Contents lists available at ScienceDirect

Remote Sensing of Environment

journal homepage: www.elsevier.com/locate/rse

Augmenting daily MODIS LST with AIRS surface temperature retrievals to estimate ground temperature and permafrost extent in High Mountain Asia

Kyung Y. Kim [a,*], Ryan Haagenson [b], Prakrut Kansara [a], Harihar Rajaram [b], Venkataraman Lakshmi [a]

[a] The Department of Civil and Environmental Engineering, University of Virginia, Charlottesville, VA, USA
[b] The Department of Environmental Health and Engineering, Johns Hopkins University, Baltimore, MD, USA

ARTICLE INFO

Edited by Menghua Wang

Keywords:
Permafrost
MODIS land surface temperature
AIRS surface skin temperature
High Mountain Asia

ABSTRACT

Permafrost in High Mountain Asia (HMA) is becoming increasingly vulnerable to thaw due to climate change. However, the lack of either *in situ* ground surface or borehole temperature data beyond the Tibetan Plateau prevents comprehensive assessments of its impact on the regional hydrologic cycle and local cascading hazards. Although past studies have generated estimates of permafrost extent in Central Asia, many are limited to the Tibetan Plateau, excluding the more remote reaches of the Tien Shan, Pamirs, and Himalayas. By leveraging surface temperatures from both the Moderate Resolution Imaging Spectroradiometer (MODIS) and Atmospheric Infra-Red Sounder (AIRS), this study advances further understanding of remotely sensed permafrost occurrence at high altitudes, which are prone to error due to frequent cloud cover. We demonstrate that the fusion of MODIS and AIRS products can accurately estimate long-term thermal regimes of the subsurface, with reported correlation coefficients of 0.773 and 0.560, RMSEs of 0.890 °C and 0.680 °C, and biases of 0.003 °C and 0.462 °C, respectively, for the ground surface and the depth of zero annual amplitude, during a reference period of 2003–2016. Furthermore, we provide a range of possible permafrost extents based on established equations for calculating the temperature at the top of the permafrost to demonstrate temperature sensitivity to soil moisture and snow cover. The MODIS-AIRS product is recommended to be a robust source of ground temperature estimates, which may be sufficient for inferring mountain permafrost presence in HMA. Incorporating the influence of soil moisture and snow depth, although limited by biased estimates, also produces estimates of permafrost regional areas comparable to previously reported permafrost indices. A total permafrost area of 1.69 (± 0.32) million km^2 is estimated for the entire HMA, across 15 mountain subregions.

1. Introduction

1.1. Background

Permafrost is traditionally defined as soil, rock, or any other subsurface material that remains at or below 0 °C for a minimum of two consecutive years (Harris et al., 2017). As the atmosphere warms under climate change, permafrost regions worldwide are becoming more susceptible to thaw as the rising heat propagates down and into the ground (Biskaborn et al., 2019), not only increasing the risk of infrastructure collapse associated with thaw-induced land subsidence and slope failure (Hjort et al., 2018; Li et al., 2022), but also threatening the balance of greater ecosystem services with the rapid release of carbon reserves (Christensen et al., 2004; Schuur et al., 2015; Turetsky et al., 2019). Thus, there is a need for a consistent method that may sufficiently delineate permafrost conditions. Past efforts have been devoted to determining permafrost occurrence at near global scales, but with discrepancies in both distribution and likelihoods due to differing methods (Brown et al., 1997; Gruber, 2012; Obu et al., 2019; Ran et al., 2022). Permafrost is an elusive component of the cryosphere because of the complex interplay between controlling factors such as climate, hydrology, geology, and vegetation; and inaccessibility of subsurface measurement (Smith et al., 2022). Additional studies on permafrost distribution are therefore warranted to generate not only a more comprehensive understanding of permafrost itself, but its relationship to near surface variables.

This is especially the case for the High Mountain Asia (HMA) region, which spans the mid-latitudes from 26 to 44° N and is affected by

* Corresponding author.
E-mail address: kk7xv@virginia.edu (K.Y. Kim).

https://doi.org/10.1016/j.rse.2024.114075
Received 4 August 2023; Received in revised form 14 February 2024; Accepted 19 February 2024
Available online 11 March 2024

microclimates at multiple scales due to the region's steep mountainous topography, resulting in ground surface temperatures that may vary >10 °C within a single kilometer (Riseborough et al., 2008; Gruber et al., 2017). HMA is also characterized by heterogeneity in precipitation regimes, ranging from the summer monsoons that dominate the Eastern Himalayas to the winter westerlies that impact the Hindu Kush and Karakoram, contributing a pattern of bimodality, whose influence on permafrost regimes is not fully understood (Gruber et al., 2017). Maintaining the largest permanent ice cover after the North and South Poles, this "water tower" supports over 10 major river basins for more than one billion people, and therefore, is a critical area of interest (Immerzeel et al., 2010; Bolch et al., 2019). Accounts of elevation-dependent warming in this region only further strengthen the rationale for regular permafrost assessments now and into the future (Pepin et al., 2015; Li et al., 2020a, 2020b). Unfortunately, very few systematic studies on permafrost have been conducted outside the Tibetan Plateau (*e.g.*, in the Tien Shan, Pamirs, and Himalayas) (Ran et al., 2012; Wang and French, 1995; Wu et al., 2013; Zou et al., 2017; Cao et al., 2019a; Zheng et al., 2020)—in part due to hazardous terrain and weather conditions that render *in situ* data collection extremely challenging (Schmid et al., 2015; Gruber et al., 2017).

Thus, remote sensing technologies have become invaluable to many surface observing studies on HMA (Stigter et al., 2017; Wan, 2014; Zou et al., 2017; Lu et al., 2020). For example, the use of optical and microwave sensors onboard Earth observing satellites (*e.g.*, the Landsat series and the Advanced Spaceborne Thermal Emission and Reflection Radiometer [ASTER]) have allowed for robust delineations and evolutions of retreating and advancing glaciers (Kääb et al., 2005; Bolch et al., 2012; Bolch et al., 2019; Shean et al., 2020). In the realm of permafrost and seasonally frozen ground (SFG), the long-term availability of land surface temperature (LST) data products from Moderate Resolution Imaging Spectroradiometers (MODIS) on board NASA's Terra and Aqua satellites (Wan, 2014) at high spatial and temporal resolution (1 km; twice daily) has become an established alternative to the use of mean annual air temperature (MAAT) and its assumed relationships with the mean annual ground temperature (MAGT) for permafrost delineation (Hachem et al., 2009; Hachem et al., 2012; Westermann et al., 2015; Zou et al., 2017; Cao et al., 2019a; Obu et al., 2019).

1.2. Permafrost maps for the northern hemisphere

In the absence of borehole measurements, the MAGT and permafrost occurrence are typically evaluated with MAATs based on air temperatures from weather stations or model outputs and assumed thermal offsets between the MAGT and MAAT. For example, Gruber (2012) offers a global permafrost zonation index (PZI), which estimates the distribution of permafrost extent (PE), defined as the probability that the MAGT within a pixel is less than or equal to 0 °C, or the fractional area of that pixel in which permafrost occurs. Gruber (2012) calculation of the PZI incorporates a MAAT based on monthly reanalysis data from the National Centers for Environmental Prediction and National Center for Atmospheric Research (NCEP/NCAR) and Climatic Research Unit gridded Time Series (CRU TS) 2.0 from a reference period of 1961–1990, resampled to a 30 arc-second gridded Shuttle Radar Topography Mission (SRTM) elevation dataset. The PE is then calculated as a function of the MAAT based on assumed empirical normal distributions for the offset, MAGT-MAAT. It is important to note that Gruber (2012) PZI does not directly incorporate the influence of either snow or land cover when accounting for the offset between MAGT and MAAT. Seasonal snow depth and vegetation are key components in process-based thermal modeling, because of their insulating and cooling influences, respectively, as barriers between the soil and air during the winter and summer (Smith and Riseborough, 2002; Zhang, 2005; Zheng et al., 2020). In addition, the reliance on MAAT and lapse rate calculations is unable to capture localized cold pooling in valleys and temperature inversions, which may be directly observed with remotely sensed data (Mutiibwa et al., 2015; Adolph et al., 2018; Collados-Lara et al., 2021; Noad and Bonnaventure, 2022). Because the distribution of surface temperatures varies diurnally, a constant lapse rate for modeling temperatures may induce additional bias (Dutra et al., 2020; Karki et al., 2020; Sun et al., 2022). MODIS can directly observe the energy of the radiating surface, which may reveal such temperature inversions, during which the surface air and ground surface temperature are effectively decoupled (Mutiibwa et al., 2015; Adolph et al., 2018). However, validation is important to assess the impact of microclimates and sub-pixel scale variability in the MODIS LST product (Collados-Lara et al., 2021).

MODIS-based LST has become a popular dataset for inferring permafrost probabilities using long-term averages of the ground surface's total freezing and thawing degree days (FDD [days · ≤ 0 °C] and TDD [days · >0 °C]) (Zou et al., 2017; Cao et al., 2019a; Obu et al., 2019). Obu et al. (2019) leveraged daily MODIS Aqua (MYD11) and Terra (MOD11) to estimate the MAGT using the CryoGrid 1 model (Gisnås et al., 2013) based on a temperature-at-the-top-of-permafrost (TTOP) approach, previously devised by Romanovsky and Osterkamp (1995, 2000) and Smith and Riseborough (1996, 2002), using FDDs and TDDs scaled by surface (nival) and thermal (conductivity) factors based on snow depth and land cover, respectively. One of the major challenges in using MODIS LST products is that they are only available for clear-sky conditions, and so, the dataset in that study is gap-filled with European Centre for Medium-Range Weather Forecasts (ECMWF) *Re*-Analysis (ERA)-Interim surface air temperatures (originally at a 0.75° spatial resolution) that are downscaled to about 1 km using sub-grid atmospheric lapse rates (Fiddes and Gruber, 2014). A permafrost occurrence fraction was then generated based on 200 ensemble runs of the CryoGrid 1 model, which calculates the FDD and TDD based on randomly drawn samples of land cover and mean annual snow depths to generate semi-empirical adjustment factors. Their land cover input was primarily based on the European Space Agency (ESA) Landcover Climate Change Initiative [CCI] project, while the modeled annual snow depths were converted from calculated mean annual snow water equivalents from a snow model forced with ERA-interim precipitation and surface air temperature fields and an empirical equation for estimating snow density (Obu et al., 2019).

Statistical models for permafrost delineation have also gained prominence with the proliferation of machine learning algorithms. Ran et al. (2022) incorporates an ensemble of such models, building upon the work of Aalto et al. (2018), to estimate permafrost occurrence probability, MAGT, and active layer thickness (ALT) trained and validated on 1002 *in situ* borehole and 452 ALT measurements across the northern hemisphere. The borehole measurements used in their analysis were taken primarily at the depth of zero annual amplitude (DZAA) and employed to produce permafrost zonation maps based on hydrothermal conditions. Ran et al. (2022) adopts this classification method to not only be more precise in characterizing permafrost types, but also acknowledge the unique nature of mountain permafrost, which cannot be easily categorized into the continuous, discontinuous, sporadic, and isolated classes due to mountain morphology (Péwé, 1983; Harris et al., 2017). Their input variables include climatological (precipitation and solar radiation) data from WorldClim (1 km), MODIS-based FDD & TDD (1 km) from Obu et al. (2019), half-monthly MODIS/Advanced Very-High-Resolution Radiometer (AVHRR)-based snow cover duration (0.05°), eight-day leaf area index (1 km) data, and soil properties (soil organic content, bulk density, and coarse fragment content) from SoilGrids250. Approximately 300 of the borehole sites are in the HMA region, with the majority (>290) located in the Qinghai-Tibetan Plateau and the remaining few in the Tien Shan. Therefore, the likelihood of overfitting their MAGT in HMA to the Tibetan Plateau's climate and topography cannot be resolved without a more extensive spatial record of *in situ* measurements across HMA's remote southern and western mountain regions.

1.3. Motivation

A combination of poor retrievals and missing data during cloudy conditions induces biases in MODIS LST datasets with prominent errors (Westermann et al., 2015; Adolph et al., 2018). Therefore, MODIS-based products must undergo some version of a gap-filling process to estimate LST during periods of cloud cover (Westermann et al., 2015). The current standard for gap-filling MODIS LST ranges from spatial and temporal spline interpolations with the highest quality data (Metz et al., 2017; Zhang et al., 2022) to supplementing missing pixels with downscaled modeled reanalysis surface temperature, which is the logic behind incorporating ERA-Interim air temperatures by Obu et al. (2019) and Ran et al. (2022). However, the coarse resolution of model outputs (*e.g.*, 0.75° for ERA-Interim) and the questionable accuracy of some MODIS pixels in cloudy conditions prevent its full exploitation. Because MODIS LST estimates can identify temperature inversions in areas greater than or equal to 1 km (Mutiibwa et al., 2015; Adolph et al., 2018; Collados-Lara et al., 2021), they are critical for monitoring ground temperatures and estimating MAGT, which may exhibit different long-term averages compared to MAATs at the same locations.

In this study, we provide robust estimates of permafrost zonation across the HMA using MAGTs derived from the complementary integration of daily surface temperature estimates from MODIS and its sister sensor onboard the Aqua satellite, the Atmospheric Infra-Red Sounder (AIRS), which can estimate temperatures below fractional cloud cover based on a well-established cloud-clearing algorithm (Susskind et al., 2003; Susskind et al., 2011; Susskind et al., 2014; Smith and Barnet, 2023).

We propose an alternative and potentially more accurate approach, which augments the MODIS LST data with AIRS surface skin temperature products, which have the same daily overpass times as MYD11. This gap-filling approach is the more robust option to either interpolating with contaminated and missing LST data or incorporating modeled rather than observed outputs. AIRS estimates still have a coarse resolution (1°) relative to MODIS LST (1 km), however, they may provide more accurate near surface temperatures than modeled outputs because they complement MODIS in real-time. The AIRS skin surface temperature observations below cloud cover provide important context due to temperature inversions and localized cool pooling, which frequently occur in mountainous and cold environments (Vitasse et al., 2017; Hearty et al., 2018; Karki et al., 2020; Collados-Lara et al., 2021; Noad and Bonnaventure, 2022). Although retrieved in infrared wavelengths (4.0 to 3.76 μm), AIRS products have undergone a cloud-clearing algorithm (initialized by an estimate generated from a neural net and observed clear-column radiances) that determines surface skin temperatures below cloud cover (Susskind et al., 2003; Susskind et al., 2011; Susskind et al., 2014).

As noted above, both snow depth and land cover exert a major influence on ground thermal regimes and permafrost occurrence. The upper and lower bounds of permafrost regional areas are calculated using offset factors based on monthly HMA-specific snow depths (Liu et al., 2021) and volumetric soil moisture from both Global Land Data Assimilation System (GLDAS)-v2.1 and ERA5-Land, which are further assessed with *in situ* data. While the previously mentioned works have either employed modeled mean annual snow depths (Obu et al., 2019) or solely snow cover data (Ran et al., 2022), a customized snow depth data product has recently become available (Liu et al., 2021), which allows for a more thorough comparison across permafrost estimates specific to HMA. The daily snow reanalysis data product (500 m spatial resolution) developed by Liu et al. (2021) assimilates an ensemble of remotely sensed data products from Landsat, MODIS, AVHRR, and SRTM with meteorological forcing from Modern-Era Retrospective analysis for Research and Applications, version 2 (MERRA-2) for water years 2000 through 2017 using a Bayesian framework (Margulis et al., 2019). Although an experimental product, this snow reanalysis dataset, which is informed by remotely sensed retrievals, offers additional insight on permafrost extent in HMA, which suffers from a lack of *in situ* observations.

Thermal conductivity is a key component in regulating the ground thermal state, which is highly dependent on both soil moisture and temperature conditions (Lunardini, 1981; Romanovsky and Osterkamp, 1995; Smith and Riseborough, 1996; Romanovsky and Osterkamp, 2000). Compared to previous approaches, which rely on land cover (Obu et al., 2019), the Normalized Difference Vegetation Index (Cao et al., 2019a), or a combination of gridded climatology, vegetation, soil properties (Ran et al., 2022) to account for the thermal offset, we employ soil moisture datasets from both GLDAS-v2.1 (Noah) and ERA5-Land, which are cited to be consistent products relative to other available reanalysis data, to represent dynamic thermal conductivities (Rodell et al., 2004; Muñoz-Sabater et al., 2021; Wu et al., 2021). Because MODIS LST products are already informed by land cover through emissivity values mapped to a specific class based on optical data, the thermal conductivity ratios determined from modeled soil moisture conditions are assumed to be more informative in estimating subsurface temperatures than incorporating vegetation extent, especially because of the lack of tall, dense vegetation at elevations where permafrost is probable and the proportionally greater effect of seasonal snow depth on the ground's long-term thermal state (Smith and Riseborough, 2002).

The incorporated methodology is described in Section 2 with a flowchart presented in Fig. 1 and datasets summarized in Tables 1 and 2, which are described further in its subsections. We also present detailed comparisons of our new PZI estimates for the HMA with the previously reported indices mentioned above. Modern PZI estimates have yet to be cross-compared for HMA, where MAGT estimates can vary greatly due to not only topographically induced microclimates, but also because previously reported MAGT estimates correspond to different depths. Results from our alternative MODIS-AIRS based PZI estimates and previous PZIs are summarized in Section 3. In Section 4, we discuss how remotely sensed LST and a few additional parameters may be sufficient for robust permafrost zonation in high altitude regions with predominantly warmer permafrost such as HMA, and review the main conclusions of our study in Section 5.

2. Datasets & methodology

2.1. MODIS-AIRS ground temperature

The primary dataset used in this study is the daily LST estimate produced from Terra and Aqua MODIS sensors (MOD11 and MYD11, respectively) (Table 1; Fig. 1). MOD11 and MYD11 are validated products that use a generalized split-window algorithm, which corrects for atmospheric effects using differential absorption of brightness temperatures captured by MODIS bands 31 (11.03 μm) and 32 (12.02 μm) and fixed surface emissivity based on a MODIS-derived land cover classification, to retrieve LST pixel values under clear-sky conditions twice a day (10:30 am/pm and 1:30 am/pm equator overpasses) (Li et al., 2013; Wan and Dozier, 1996; Wan, 2014). It is documented to have a mean error within ±1.0 K in all validation sites, except for one in a bare soil region with a mean error of ±1.9 K (Wan, 2014). Only pixels flagged with ≤1 K error were selected at the cost of additional—potentially invalid—observations for both MOD11 and MYD11.

As noted above, gap-filling was performed based on a fusion of AIRS surface skin temperature and MODIS LST scenes. Given that MODIS LST estimates are only available in clear sky conditions, nudging the surface energy balance towards a warmer LST average, or erroneously capturing cooler temperatures atop clouds that have not been appropriately filtered out, a gap-filling technique is required to address both cold and warm biases generated from daily MODIS LST estimates alone. The downscaling method for AIRS surface temperature circumvents this issue in two-ways: first, it eliminates out the discrepancies in daily LST estimates due to cloud cover, and second, it reveals temperatures below fractional cloud cover with its physics-informed cloud-clearing algo-

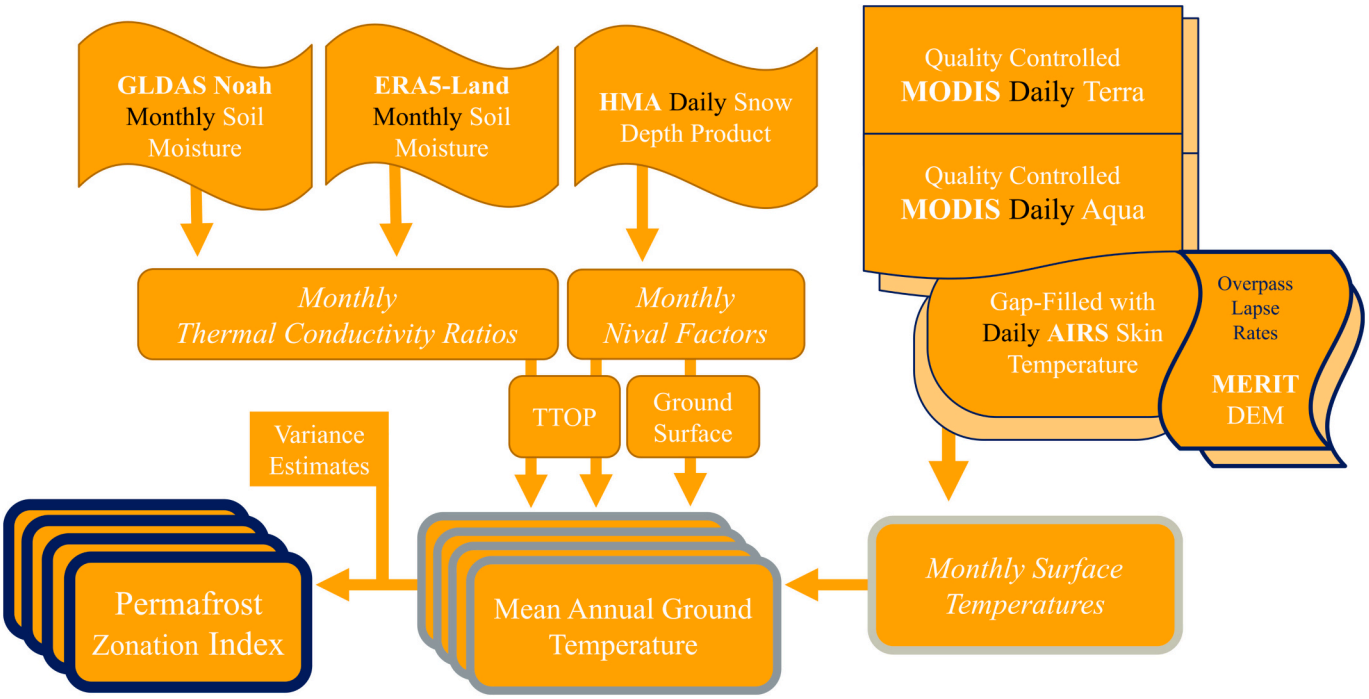

Fig. 1. This workflow was used to generate the final PZIs (permafrost zonation indices). Complementary methods for the thermal offset were compared when calculating the TTOP (temperature-at-the-top-of-permafrost) (MAGT-IIIa,b) and snow depth-corrected MAGT (mean annual ground temperature) (MAGT-II). The daily remotely sensed products from MODIS and AIRS included observations from both AM and PM overpasses. Four different PZIs were generated for comparing across the MAGT estimates. The sub-grid variance of MERIT DEM and validation-based errors were incorporated in the final step to compute the variance associated with the MAGT estimates (Eq. (8)).

Table 1
Data products used for this study's MAGT (mean annual ground temperature) and PZI (permafrost zonation index) models.

Variable	Product	Availability	Temporal Resolution	Spatial Resolution	Citation
Land Surface Temperature	MOD11	02/24/2000 – Present	Daily (x2)	1 km	Wan, 2014
	MYD11	07/04/2002 – Present			
	Gap-Filled MYD11	01/2003–12/2020			Zhang et al., 2022
Surface Skin Temperature	AIRS ST	08/31/2002 – Present	Daily (x2)	1°	Susskind et al., 2014
Elevation	MERIT DEM	01/01/1987–01/01/2017	–	90 m	Yamazaki et al., 2017
Snow Depth	HMA Snow Reanalysis	10/01/1999–09/30/2017	Daily	500 m	Liu et al., 2021
Soil Moisture 0–200 cm	GLDAS Noah	01/2000 - Present	Monthly	0.25°	Beaudoing and Rodell, 2020
0–289 cm	ERA5-Land	01/1950 – Present	Monthly	9 km	Muñoz-Sabater et al., 2021
Snow Cover	MOD10A1	02/24/2000 – Present	Daily	500 m	Riggs and Hall, 2015
	MYD10A1	07/04/2002 – Present			
Glaciers	GLIMS Database	01/01/1850 - Present	Varies	Varies	GLIMS and NSIDC, 2018
Lakes	TP Lake Dataset	1960s, 2005, 2014	Varies	Varies	Wan et al., 2016

rithm (Susskind et al., 2014). Multivariate linear regressions were generated on an overpass (am/pm) basis with the AIRS temperature estimates against the Multi-Error-Removed Improved-Terrain (MERIT) Digital Elevation Model (DEM) (Yamazaki et al., 2017)—noted to be the most dependable elevation model for the HMA region by Liu et al. (2019)—resampled to a 1° (approximately 111 km) resolution, and their latitudes. The coefficients were then applied to a resampled 1 km MERIT DEM to produce a downscaled AIRS surface skin product as represented by Eq. (1).

$$\mathrm{AIRS}_{\mathrm{GF}} = \beta_0 + \beta_1 \mathrm{elevation} + \beta_2 \mathrm{latitude} \quad (1)$$

Where β_0 is the skin temperature estimate for the 1° pixel, β_1 is the coefficient for elevation (*i.e.*, the lapse rate), β_2 is the coefficient for latitude, which provides information with respect to the distribution of heat due to insolation or potentially mesoscale atmospheric circulation in the linear model, and $\mathrm{AIRS}_{\mathrm{GF}}$ is the downscaled 1 km surface skin temperature product used for gap filling the MYD11 data.

The AIRS surface skin temperatures were effectively downscaled with a unique combination of coefficients for each retrieved overpass. These coefficients may be interpreted as lapse rates fixed by both elevation and latitude. Boxplots of the modeled coefficients of determination (R^2) and parameters for downscaling all PM and AM retrievals are available in the supplementary text (Supplementary Fig. S1). The R^2 values were higher for the nighttime than the daytime scenes, whose medians were about 0.90 and 0.65, respectively. The 1 km surface temperatures were then gap-filled for pixels with null values for each matching overpass in the MYD11 dataset. The two MOD11 retrievals per day were averaged with the gap filled MYD11 AM and PM retrievals to retain additional information obtained by MODIS on a monthly timestep.

Monthly averages of LST are used to standardize the dataset in terms of sampling frequency. Although degree-days have traditionally been used to generate annual freezing and thawing indices, monthly temperature variations have been shown to adequately capture the integrated thermal influence of climatology on subsurface temperatures, especially in the context of limited data availability (Lunardini, 1981;

Table 2
In situ data sources used for accuracy assessments. The numbers left of the depth column denote the count of validation sites.

Network and Sources	Snow Depth	Soil Moisture	Surface Air	Ground Surface	Borehole	Depth (m)	Time Period (frequency)
NOAA GHCN (Menne et al., 2012)	46	–	90	–	–	–	1915 – Present (Daily)
Wu et al., 2012	–	–	–	–	27	12–15	2006–2010 (Average)
Wu et al., 2015	–	–	–	–	10	0.5–15	2002–2012 (Average)
Qin et al., 2017	–	–	–	–	46	10–15	2011–2013 (Average)
Wang et al., 2017	–	–	–	–	2	14	2012–2014 (Average)
Luo et al., 2018a	–	–	–	17*	14	0.05–3	2011–2016 (Average)
Sun et al., 2018	–	–	–	–	28	10–20	2006–2013 (Average)
GTN-P (Biskaborn et al., 2019)	–	–	–	–	12	7.5–40	2007–2016 (Annual)
HiWAT (Che et al., 2019)	1	9	9	9	–	0–2	2013–2017 (Half-Hourly)
Ma et al., 2020	–	6	6	6	–	0–2	2002–2019 (Hourly)
Wani et al., 2020	1	–	–	24	–	0.1	2016–2017 (Average)
ICIMOD and NVE, 2021a–d; ICIMOD, 2021	4	–	4	39	–	0	2014–2020 (Hourly)
ISMN (Dorigo et al., 2021)	–	118 (50)	–	118	–	0.05 (80)	2008 – Present (Hourly)
Zhao et al., 2021	–	11	5	11	84	0.1–20	2002–2019 (Hourly to Annual)
Total Sites	52	144	114	224	223		

* The ground surface temperatures (GST) from this study were only included for the mean annual validations, and not daily or monthly GST validations.

Boyd, 1976; Wu et al., 2011; Wang et al., 2019). The monthly surface temperatures (MST) derived from daily surface temperature products as described in Eq. (2) were then averaged to the mean annual ground temperature at the surface, denoted from now on as MAGT-Ia (see Table 3 for all MAGT acronyms used).

$$MST_{GF} = \frac{\sum_{i=1}^{n} \mathrm{MYD11AIRS}_{AM,i} + \mathrm{MYD11AIRS}_{PM,i} + \mathrm{MOD11}_{AM,i} + \mathrm{MOD11}_{PM,i}}{n} \quad (2)$$

All surface temperature products were validated at both a daily and monthly frequency at a total of 114 surface air and 207 ground surface sites from 2003 through 2016 (Table 2). The assessment was able to compare errors across products and confirm the quality issues related to MODIS-based LST products.

2.2. Stationary assumption and tests

Stationarity over the period 2003–2016 must be assumed to generate a normally distributed probability density function for MAGT (Ia). If inherent trends (*e.g.*, warming) exist, calculated permafrost extents may be less robust due to the shifting mean within the reference period. The condition for stationarity of annual surface temperatures in HMA's subregions was therefore assessed using the Augmented Dickey-Fuller (ADF) and Kwiatkowski–Phillips–Schmidt–Shin (KPSS) tests. The ADF test's null hypothesis states that a given time series contains a unit root suggesting non-stationarity, but is stationary post first-differencing (Harris, 1992); the KPSS test's null hypothesis is the opposite, *i.e.*, the time series is hypothesized to be trend-stationary with the absence of a unit root (Kwiatkowski et al., 1992). If the null hypothesis is rejected under the ADF test, the time series is stationary because a unit root results in residuals with non-constant mean and variance over time without differencing. Spearman's rank correlation coefficients were also calculated to determine the strength of a monotonic trend if present. Resulting metrics for the ADF, KPSS, and Spearman's rank tests are available in Table 4. Each mountain subregion was digitized based on cursory elevation patterns with MERIT DEM and informed by the boundaries used in Bolch et al. (2019) and Furian et al. (2021).

Stationarity statistics of the HMA regions based on the ADF and KPSS tests are shown in Table 4. Most regions failed to reject the null hypothesis at a 5% significance level, implying non-stationarity based on the ADF values; however, the Tibetan Plateau interior and mountains to the West (Hindu Kush, Pamir, Hissar Alay) exhibited stationarity. The KPSS test implies stationarity for regions that rejected the null hypothesis at a 5% significance level, which include the Hengduan and Nyainqentanglha. The Spearman's rank statistics determine that a significant monotonic trend exists for the Hengduan and Nyainqentanglha, but also the Tibetan Plateau, which had shown stationarity with the previous two tests.

The derivation of PZIs assumes a stationary climate and some caution must be exercised in the use of MODIS LST and air temperature data due to contemporary warming. A detailed evaluation of stationarity in MODIS LST is presented in Section 3.2 below.

Table 3
Calculated MAGTs (mean annual ground temperature) and their descriptions. The following acronyms are used: MODMYD11-AIRS (MODIS Terra and Aqua land surface temperature gap-filled with downscaled AIRS surface temperature), HMA (High Mountain Asia), TTOP (temperature-at-the-top-of-permafrost), DZAA (depth of zero annual amplitude), PZI (permafrost zonation index).

MAGT	Datasets	Notes
Ia	MODMYD11-AIRS	Land surface without any offset
II	MODMYD11-AIRS; HMA Snow Reanalysis	Land surface with nival offset
IIIa	MODMYD11-AIRS; HMA Snow Reanalysis; GLDAS-Noah	TTOP based on soil moisture
IIIb	MODMYD11-AIRS; HMA Snow Reanalysis; ERA5-L	TTOP based on soil moisture
IIIc	Obu et al., 2019	TTOP based on land cover
IV	Ran et al., 2022	DZAA using training data
Ib	Gruber, 2012	Air surface with assumed offset (only PZI available)

2.3. Temperature offset corrections

The LST as detected by MODIS is a function of the observed surface emissivity and therefore cannot estimate surface temperatures below snow, whose emissivity varies with depth, grain size and density (Wan and Dozier, 1996). However, the MAGT calculation is a first step in the refined estimation of ground temperatures to account for the influence of snow cover and at various depths. To represent the insulating effect of snow cover, a reliable snow depth dataset is necessary. Liu et al. (2021) offers a daily snow reanalysis product (500 m) specific to the HMA region based on a spatially distributed land surface model-snow depletion curve by Margulis et al. (2019), which assimilates remotely sensed Landsat and MODIS-derived fractional snow cover area with an

Table 4
Stationarity tests of mountain regions based on MAGT-Ia (2003–2016). Metrics for rejected null hypotheses are bolded.

Region	ADF Test statistic | *p*-value | 5%			KPSS Test statistic | p-value | 5%			Spearman's Rank statistic | p-value	
Hengduan	−2.432	0.133	−3.127	**0.555**	**0.029**	0.463	**0.631**	**0.016**
Hindu Kush	**−3.877**	**0.002**	−3.127	0.160	0.100	0.463	0.218	0.455
Hissar Alay	**−4.195**	**0.001**	−3.127	0.166	0.100	0.463	0.297	0.303
Himalaya	−2.107	0.242	−3.290	0.259	0.100	0.463	0.284	0.326
Altun	−1.125	0.705	−3.290	0.364	0.093	0.463	0.442	0.114
Qilian	1.699	0.998	−3.290	0.458	0.052	0.463	0.525	0.054
Tien Shan	−1.527	0.520	−3.367	0.215	0.100	0.463	0.305	0.288
Bayan Har	−2.759	0.064	−3.127	0.290	0.100	0.463	0.468	0.091
Nyainqentanglha	−2.543	0.105	−3.127	**0.498**	**0.042**	0.463	**0.547**	**0.043**
Pamir	**−3.249**	**0.017**	−3.127	0.388	0.083	0.463	0.508	0.064
Kunlun	1.873	0.998	−3.290	0.352	0.098	0.463	0.516	0.059
Gandise	−1.080	0.723	−3.290	0.279	0.100	0.463	0.358	0.208
Tanggula	−2.507	0.114	−3.127	0.420	0.069	0.463	0.464	0.095
Tibetan Plateau	**−3.206**	**0.020**	−3.127	0.347	0.100	0.463	**0.543**	**0.045**
Karakoram	−0.587	0.874	−3.290	0.317	0.100	0.463	0.459	0.098

ensemble of meteorological forcing, topographic (SRTM and ASTER), and land cover data (AVHRR). An accuracy assessment was also performed with available monthly snow depth measurements at 52 sites, with most data sourced from the National Oceanic and Atmospheric Administration's (NOAA) Global Historical Climatology Network (GHCN) (Menne et al., 2012). Although data over areas where only seasonal snow is present are reportedly more accurate, pixels containing more persistent snow cover were included in the analysis to achieve maximal coverage (Liu et al., 2021). Glaciers were masked out based on a rasterized inventory from the Global Land Ice Measurements from Space (GLIMS) database (GLIMS and NSIDC, 2018).

Daily snow depth estimates were averaged to a monthly time step, linearly resampled to the 1 km resolution of the MODIS LST, and ultimately used as inputs for the two MAGT equations based on the TTOP approach. The first method only incorporates the snow depth-dependent winter scaling factor, *i.e.*, the nival offset, to estimate MAGT influenced by snowpack (MAGT-II, Table 3), as shown in Eq. (3):

$$\mathrm{MAGT-II} = \frac{(It) + (nf^{*}If)}{P} \tag{3}$$

Where *If* equals the frozen degree index (in month-degrees, or the cumulative sum of $\mathrm{MST_{GF}} \leq 0$), *It* equals the thawing degree index (in month-degrees, or the cumulative sum of $\mathrm{MST_{GF}} > 0$), and, *nf* (nival offset) is a snow depth-dependent winter scaling factor based on MAGT-

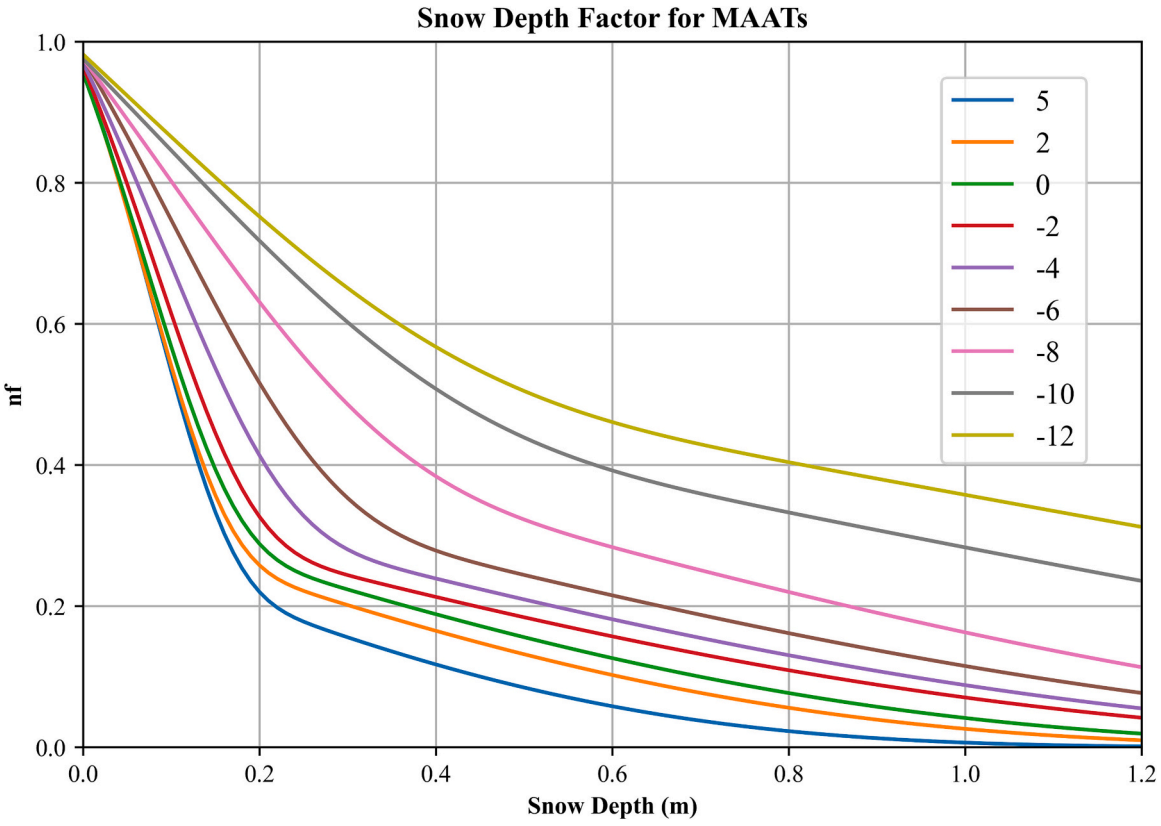

Fig. 2. The nival factors (nf) for the winter season (snow depth correction) were estimated by fitting curves from Smith and Riseborough (2002). A double exponential function was selected to be the best fitting curve, and four parameters (a, b, c, d) were calculated for each MAAT (mean annual air temperature, °C) curve (Eq. (4)). However, given that this study uses monthly gap-filled surface temperatures to correct for the snow depth, MAGT-Ia was substituted in place of the designated MAAT.

Ia (Fig. 2), and *P* equals the period, or 12 for monthly means.

$$nf_{MST} = e^{a\left(e^{b*MSD}\right)} + e^{c\left(e^{d*MSD}\right)} \quad (4)$$

Where *a*, *b*, *c*, *d* are parameter values (Table 5) fitted to the *nf* curves from Smith and Riseborough (1996, 2002) shown in Fig. 2, and *MSD* is the monthly averaged snow depth given a binned MAGT-Ia threshold; for example, temperatures >5 °C were binned to the 5 °C curve, temperatures ≥2 °C & <5 °C were binned to the 2 °C curve, … temperatures ≥ −12 °C and < −10 °C or < −12 °C were binned to the −12 °C curve. From Fig. 2, note that the *nf* at the same snow depth is lower in areas with higher MAATs. Therefore, snow depths have a greater effect on ground temperature in areas with higher mean annual temperatures.

The thermal conductivity ratio of unfrozen to frozen conditions (*rk*) can approximate the thermal offset between the ground surface and permafrost table caused by seasonal, transient heat transfer (by conduction) and soil moisture conditions. This value is largely influenced by unfrozen water, which is only about a quarter as thermally conductive as ice and hinders heat transport in thawed conditions (Lunardini, 1981; Smith and Riseborough, 2002).

Eq. (5) is the method for calculating the MAGT at the top of the permafrost (MAGT-III), which includes a thermal conductivity ratio in addition to the nival offset to account for the transfer of heat between the frozen and unfrozen subsurface layers in permafrost regions.

$$\mathrm{MAGT-III} = \frac{\left(\sum_{i=1}^{12} rk*MST_{\mathrm{GF}} > 0\right) + \left(\sum_{i=1}^{12} nf*MST_{\mathrm{GF}} \le 0\right)}{12} \quad (5)$$

Thermal conductivity ratios were calculated with a simple relationship (Eq. (6)) that directly relates the thermal conductivities of water (0.56 W m^{-1} $°C^{-1}$) and ice (2.24 W m^{-1} $°C^{-1}$) to the thermal conductivity ratio, given a volumetric water content (Kersten, 1949; Lunardini, 1981; Smith et al., 2015).

$$\frac{1}{rk_i} = \frac{k_{\mathrm{F}}}{k_{\mathrm{T}}} \approx \left(\frac{k_{\mathrm{ice}}}{k_{\mathrm{water}}}\right)^{\theta_i} \quad (6)$$

Where rk_i is the monthly thermal conductivity ratio, k_{F} and k_{T} are the effective thermal conductivities of the ground, given frozen and thawed conditions, respectively, and θ_i is the monthly soil moisture estimate. Modeled soil moisture estimates from both GLDAS-Noah (IIIa) and ERA5-L (IIIb) were assessed using outputs against the corresponding *in situ* monthly soil moisture at depth, primarily from the International Soil Moisture Network (ISMN) (Su et al., 2011; Dente et al., 2012; Yang et al., 2013; Dorigo et al., 2021). However, weighted averages from each dataset across all available depths (0–10 cm, 10–40 cm, 40–100 cm, 100–200 cm for GLDAS; 0–7 cm, 7–28 cm, 28–100 cm, 100–289 cm for ERA5-L) were used for the thermal conductivity ratio estimates.

2.4. Evaluation of MAGT estimates

A total of 223 borehole and 224 seasonally frozen ground MAGTs were used to assess the accuracy of all mean annual temperatures: at the surface as detected by remote sensing (Ia), at the ground surface below seasonal snow cover (II), and at the top of the permafrost table (III).

Table 5
Fitted double exponential parameters for *nf* values.

MAGT-Ia (°C)	*a*	*b*	*c*	*d*	R^2
5	−0.40568	11.28589	−1.21495	1.41858	0.9977
2	−0.45102	10.99399	−1.12629	1.17477	0.9963
0	−0.48263	10.03079	−1.08481	1.07625	0.9960
−2	−0.47117	9.19220	−1.07925	0.89888	0.9966
−4	−0.50442	7.33974	−1.00556	0.88235	0.9967
−6	−0.54750	5.70432	−0.91973	0.85459	0.9975
−8	−0.70372	3.90016	−0.73267	0.90727	0.9983
−10	−0.63919	0.67973	−0.80309	2.91896	0.9988
−12	−0.55206	0.62161	−0.90099	2.64386	0.9986

Again, the MAGTs of the *in situ* data were assumed to be stationary for the purposes of comparing the modeled values against the observed. Ordinary least squares regression models were used to plot the data along a 1:1 line, and correlation coefficients, root mean square errors (RMSE) and biases were used as metrics for comparison.

2.5. Permafrost region estimation

All MAGTs were transformed to PE (permafrost extent) probabilities by assuming a normal distribution with standard deviation σ for the true MAGT to calculate the probability that MAGT ≤ 0:

$$\mathrm{F}_{MAGT\le 0} = \frac{1}{2}\, erfc\left(\frac{MAGT}{\sqrt{2\sigma^2}}\right) \quad (7)$$

In (7), erfc is the complementary error function, and σ^2 is the total variance associated with the calculated MAGTs (Eq. (8)).

$$\sigma^2 = \sigma_{\mathrm{t}}^2 + \sigma_{\mathrm{m}}^2 + (\lambda\sigma_{\mathrm{E}})^2 \quad (8)$$

The three components included in quantifying the uncertainty of MAGT are the climatological variance of the MAGT across the 14-year period (σ_{t}^2), the total error based on the data accuracy assessments (σ_{m}^2), and the uncertainty due to variations of elevation within the pixel $(\lambda\sigma_{\mathrm{E}})^2$. The last component is calculated as the variance of the sub-grid (90 m) elevation derived from MERIT DEM (σ_{E}^2), multiplied by the square of the mean lapse rate based on the distribution of calculated lapse rates when downscaling AIRS surface skin temperature product (λ; Fig. S1).

Permafrost regions were then calculated by classifying the permafrost extent based on standard zonation down to 0.05, below which are not considered due to the minimal likelihood and high uncertainty of permafrost cover at such percentages (Brown et al., 1997; Gruber, 2012): continuous (90% to 100%), discontinuous (50% to <90%), sporadic (10% to <50%), and isolated (5% to <10%). The zonation indices were then reprojected on the Equal-Area Scalable Earth (EASE) Grid, and all pixels were summed according to their zonation. The sums were then converted to area (km^2), based on a ratio factor associated with the EASE Grid. Finally, PZIs of the HMA region modeled by Gruber (2012), Obu et al. (2019), Ran et al. (2022), and this study were compared using a cutoff of all PE > 0.05, to compare total permafrost regional areas obtained from the varying definitions of permafrost zonation across these studies.

3. Results

3.1. Preliminary surface temperature validations

Fig. 3 affirms the accuracy of our novel gap-filling method for regions with scarce data availability. The integrated MODMYD11-AIRS surface temperature product outperforms even the most up-to-date 1 km MODIS gap-filled product produced by Zhang et al. (2022) for estimating ground surface temperature. A marginal warm bias of 0.2 °C exists through the validation period (2003–2016); however, it is a result of offsetting a cold bias from the downscaled AIRS product alone with additional MODIS observations. The MODMYD11-AIRS estimates also perform well during the monsoon season with respect to ground surface temperatures, with the least bias (0.50 °C) and highest correlation coefficient (0.83). However, this product does exhibit a warm bias in the context of surface air temperatures, which is especially high in the monsoon season (Table 6). The Zhang et al. (2022) product, while consistent, has a cold bias, likely due to the aforementioned causes of cloud contamination, that appears to perform better as a near surface air product. Validations at the daily scale are available in the supplementary text (Table S1; Fig. S2).

Figs. S3 and S4 in the supplementary material provide accuracy assessments of the soil moisture and snow depth products used to model

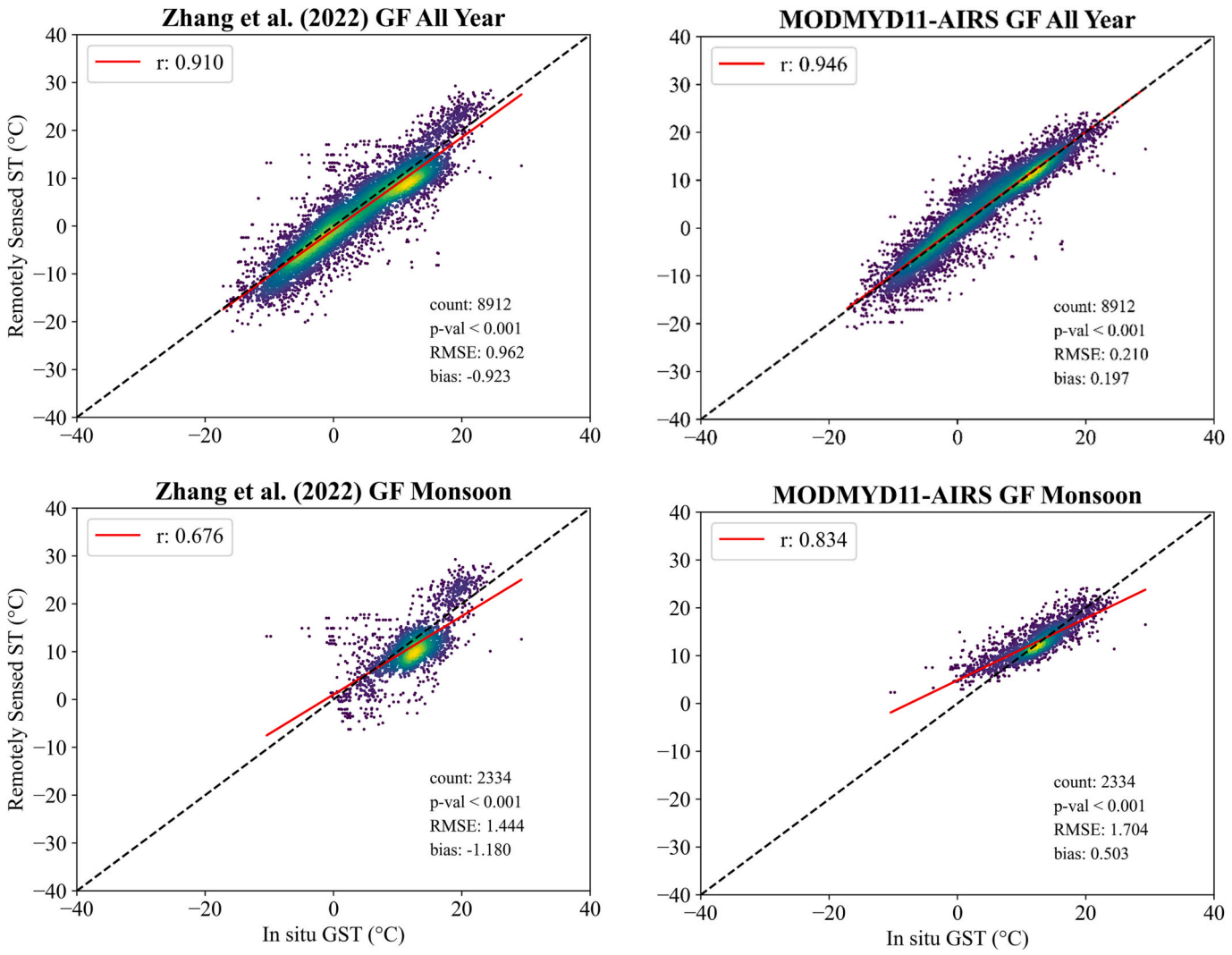

Fig. 3. Monthly averaged temperatures for two gap-filled (GF) products are validated with *in situ* ground surface temperatures (GST) using 207 sites. The temperatures generated with the combined MODIS-AIRS observations from this study perform better than the latest available gap-filled MODIS daily land surface temperature product from Zhang et al. (2022), with both lower biases and higher correlation coefficient during either the monsoon season (June—August) or for the entire year. Daily validations are provided in the Supplementary Text (Fig. S2). The dark purple to yellow gradient represents the density of points, from least to greatest. (For interpretation of the references to colour in this figure legend, the reader is referred to the web version of this article.)

Table 6
Monthly surface temperature product validation. The RSME and bias are in units of °C. The highest performing metrics are bolded.

	All Year			Monsoon Season				All Year			Monsoon Season		
Ground Surface Temperature	r	RMSE	bias	r	RMSE	bias	Air Temperature	r	RMSE	bias	r	RMSE	bias
AIRS GF (downscaled)	0.923	0.801	−0.431	0.555	3.001	0.119		0.962	2.445	2.415	0.889	3.708	3.586
MODMYD11	0.914	2.330	2.180	0.755	2.779	2.770		0.909	2.953	2.948	0.791	3.937	3.625
MODMYD11-AIRS	**0.946**	**0.210**	**0.197**	**0.834**	1.704	**0.503**		**0.968**	2.668	2.650	**0.933**	3.519	3.461
Zhang et al., 2022	0.910	0.962	−0.923	0.676	**1.444**	−1.180		0.946	**0.882**	**0.875**	0.884	**1.021**	**1.020**

the MAGT at different depths. The soil moisture estimates from ERA5-Land and GLDAS exhibited a wet bias of 0.11 m^3/m^3 and 0.02 m^3/m^3, respectively. The daily HMA Snow Reanalysis from Liu et al. (2021) also had positive bias, of about 0.08 m, which offers context for the dataset's application for modeling ground temperatures, since ground temperatures are known to be sensitive to the insulating property of snow cover (Zhang, 2005). Although reasonable performance was demonstrated when validated against snow water equivalent estimates from the Tuolumne River Watershed (elevation range of 1600–3500 m) in the Sierra Nevada of California, further studies are required to better constrain snow depth estimates for HMA (Margulis et al., 2019).

3.2. Stationarity and transect assessments

Fig. 4a shows a map of the gap-filled MAGT-Ia (2003–2016) for the HMA region, labeled with the mountain region names and *in situ* locations displayed by their associated source or study. Fig. 4b is a histogram of three (2013–2016) and four-year averages (2003–2007; 2008–2012) of the gap-filled MAGT (Ia), which shows a minor shift to warmer temperatures over time. Fig. 4c shows the annual time series of spatially averaged LST estimates for each mountain region, ordered by decreasing MAGT. Some regions appear to exhibit warming, as determined by the ADF test. Estimates from the Hengduan, Karakoram, Himalayas, Kunlun,

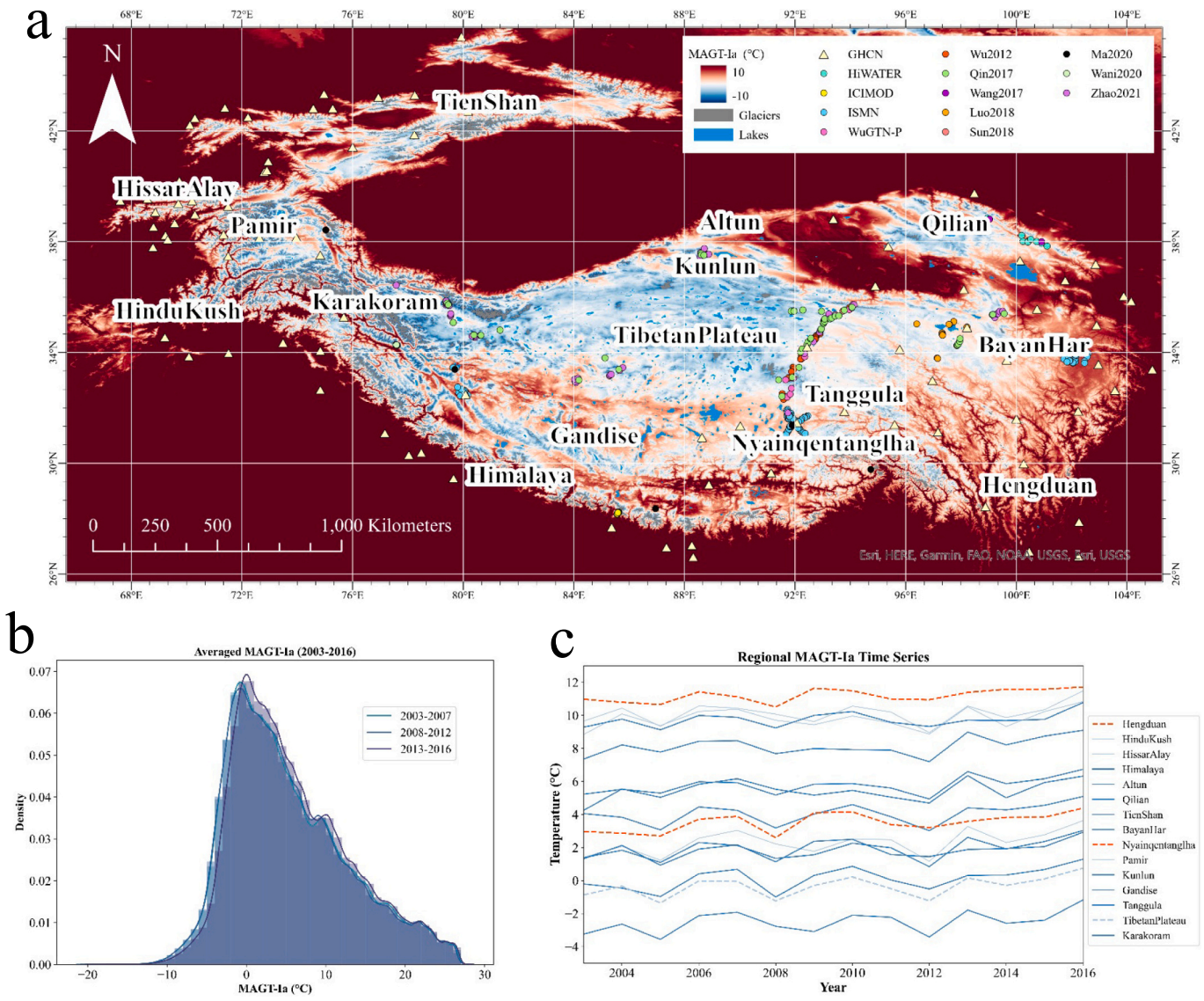

Fig. 4. a) Map of the gap-filled MAGT-Ia. b) A qualitative assessment of stationarity in MAGT-Ia time series based on frequency distributions in different periods. The MAGT (mean annual ground temperature) for 2013–2016 shows a marginal shift to the right, compared to the previous time periods (Table 4; Section 3.2). c) A time series of the gap-filled annual surface temperature from which MAGT-Ia was derived. An augmented Dickey Fuller test results in stationarity for only the Hindu Kush, Hissar Alay, Pamirs, and interior Tibetan Plateau (in light blue), however, the KPSS test resulted in stationarity in all regions except the Hengduan and Nyainqentanglha (red). Dotted lines are regions in which a significant monotonic (increasing) trend was determined by the Spearman's rank correlation coefficient, with the maximum trend occurring in the Hengduan. (For interpretation of the references to colour in this figure legend, the reader is referred to the web version of this article.)

Altun, Gandise, Bayan Har, Tanggula, Nyainqentanglha, Qilian, and Tien Shan fail to reject the null hypothesis of the ADF test at a 5% significance level (Table 4). However, the KPSS test led to an inference of trend-stationarity for most regions, except the Hengduan and Nyainqentanglha, implying these two regions are indeed warming within this period, with monotonic trends confirmed by the Spearman's rank correlation coefficients (Table 4).

Ground temperatures along transects shown in Fig. 5b are displayed as the upper subplots in Fig. 5a to compare the remotely sensed (Ia) and modeled MAGTs (including Obu et al.'s TTOP-based MAGT-IIIc [Obu et al., 2019] and Ran et al.'s MAGT-IV at the DZAA [Ran et al., 2022]). which also provide elevation data from MERIT DEM for context. Nearby glaciers coincide with points where the mean annual snow depths spike in the lower subplots of Fig. 5a with the remotely sensed (mean annual) fractional snow cover from MODIS, which the snow reanalysis product incorporated. The juxtaposition of these plots confirms three key assumptions. First, the nival and thermal offset equations from Smith and Riseborough (2002) adjust for the influence of snow cover on the land surface temperature, which is clearly shown along the transects for both the Tien Shan and Southern Himal. In contrast, shallower snow depths along the Qilian have a much more muted effect on the modeled surface ground temperature. Second, elevation has a direct effect on the modeled ground temperatures. The DEM of each transect mirrors the changes in the MAGT. Third, the depths at which the ground temperatures are modeled are discernible in the temperature profiles, with TTOP MAGTs (III) mostly exhibiting colder temperatures, compared to either the MAGT at the surface or DZAA. While ground temperatures begin to warm up with depth at the DZAA (IV) due to the geothermal gradient, the TTOP MAGT (III) is typically colder than the surface MAGT (Ia, II) because of the thermal conductivity of frozen soils at the permafrost table which causes ground temperatures to cool with depth in the active layer, creating possible subsurface conditions for permafrost even in areas where the MAAT is warmer than 0 °C (Smith and Riseborough, 2002; Smith et al., 2022). An additional transect and map for the

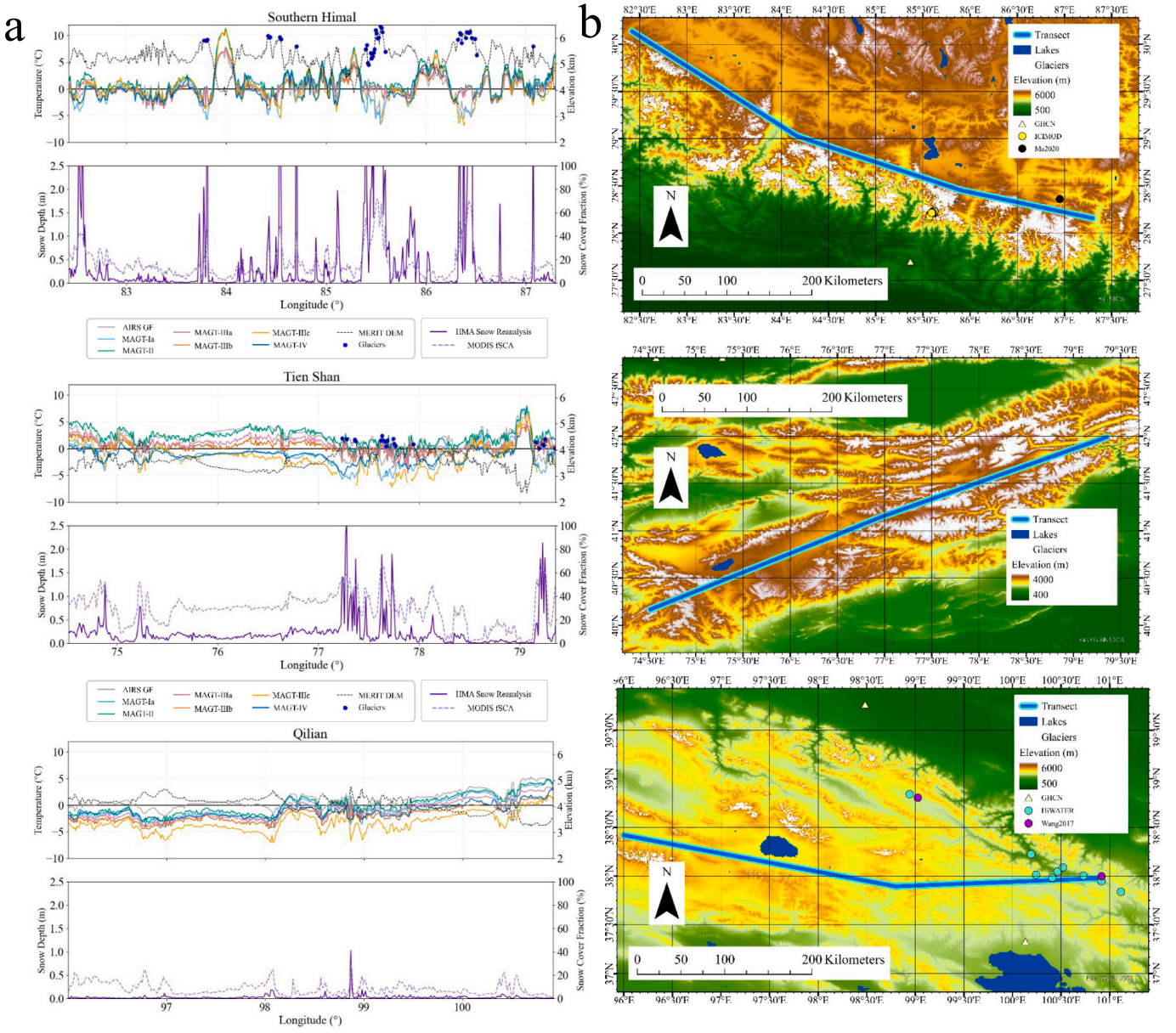

Fig. 5. a) Modeled temperature estimates along transects shown in (b): downscaled AIRS product used for GF (gap-filling) (Eq. (1)); MODMYD11-AIRS MAGT-Ia (Eq. (2)); MAGT-II (Eq. (3)); MAGT-IIIa,b (GLDAS, ERA5-L) (Eq. (5)); MAGT-IIIc (Obu et al., 2019); MAGT-IV (Ran et al., 2022), elevation (MERIT DEM), masked glaciers from GLIMS, mean annual snow depths (Liu et al., 2021), and MODIS-based fractional snow cover are plotted for the Tien Shan, Southern Himal, and Qilian transects. The subplot below each temperature plot provides context for the discrepancy between the modeled and observed temperatures due to snow. B) Inset elevation maps on the right show the transects accompanying the subplots to the left. An additional map for Western Himal is provided in the Supplementary Text (Fig. S5).

Western Himalayas are available in the supplementary material (Fig. S5).

3.3. MAGT validations

Fig. 6 shows the validation results for the generated MAGTs in this study, along with the two from literature (IIIc [Obu et al., 2019], IV [Ran et al., 2022]), against all ground measurements, including both borehole data and MAGT at different depths near the ground surface. The TTOP MAGTs (III) all show a bias towards cooler temperatures, while the MAGT-II resulting from only the snow depth correction shows a warm bias of about 0.82 °C. The MAGT-Ia without any modeled correction and the MAGT-IV from Ran et al. (2022) exhibited the lowest errors, with a total RMSE of about 0.77 °C and 1.21 °C respectively. A 0.23 °C bias exists in the MAGT-Ia product, but the MAGT-IV bias is even lower at about −0.01 °C, which is expected when validating with trained data (Ran et al., 2022). Table 7 has the validations separated by depth, with the MAGT depth of seasonally frozen ground ranging between 0.5 and 2 m across 224 sites. Most of the borehole temperatures are taken at the DZAA (between 10 and 20 m deep), except for TTOP measurements from the Luo et al. (2018a) study, which were sampled at a depth of 3 m.

Against the *in situ* borehole measurements, all of the MAGTs fared worse. The TTOP (MAGT-IIIc) from Obu et al. (2019) exhibited the poorest metrics, with the largest bias of −1.12 °C, an RMSE of 1.29 °C, and a weak statistically significant correlation coefficient of 0.36. However, it performed better against the seasonally frozen ground measurements with a stronger linear relationship (r = 0.78), despite a similar cold bias (−1.14 °C) and error metric (RMSE = 1.51 °C). Of the MAGTs from this study, the remotely sensed MAGT (Ia) product consistently outperformed the others with respect to seasonally frozen ground measurements, rivaling the results of the MAGT-IV validation with its very low bias (< 0.01 °C) and RMSE at 0.91 °C, which implies

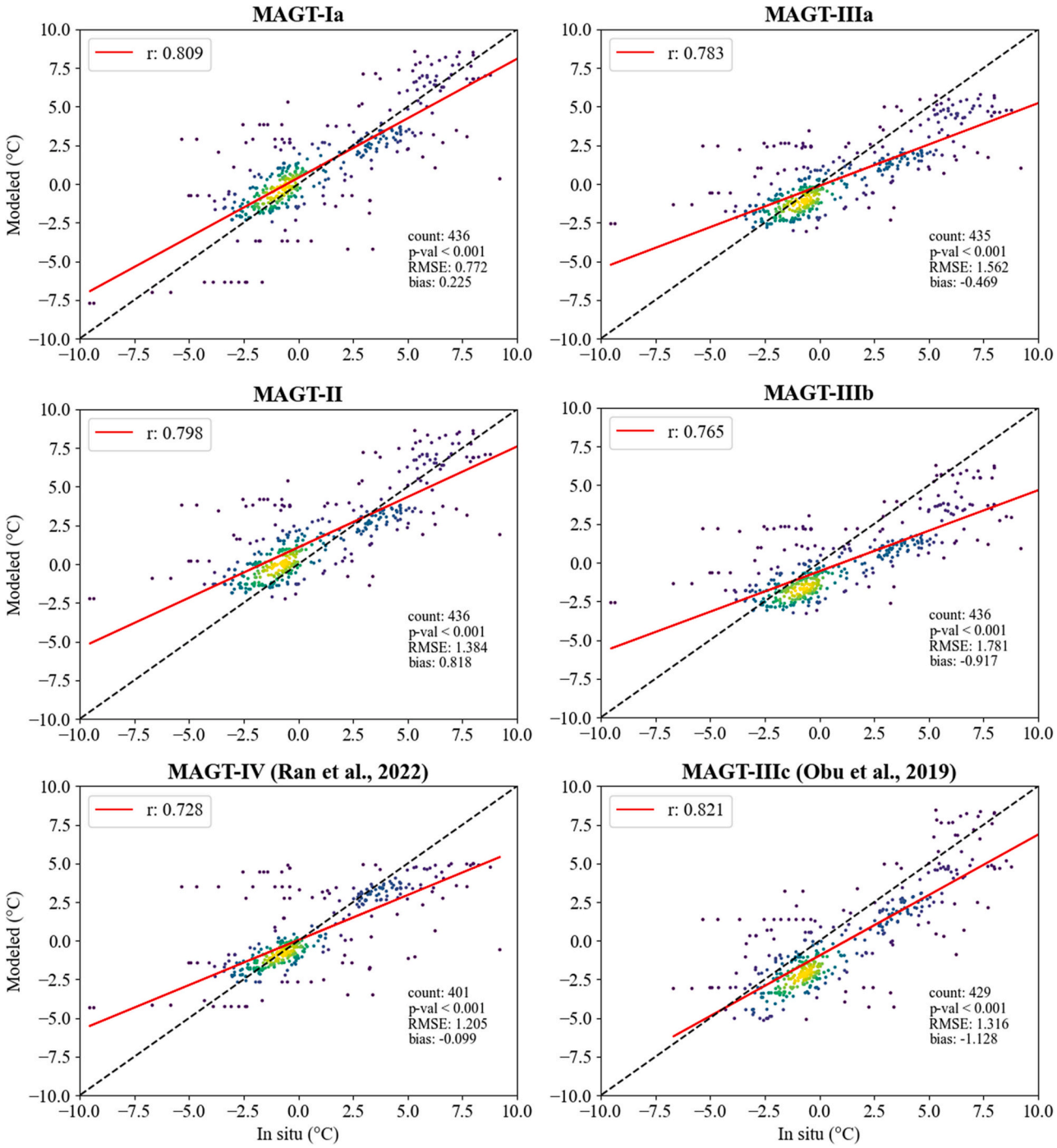

Fig. 6. All *in situ* ground temperature measurements, including those near the seasonally frozen ground surface and at the depth of zero annual amplitude or top of permafrost, were used for the validations in this figure. The MAGT (mean annual ground temperature) with the least bias was Ran et al. (2022) that was fitted to the ground measurements, but the MAGT with least variance (RMSE of about 0.8 °C) was the MAGT-Ia without any corrections. The TTOP (temperature-at-the-top-of-permafrost)-based MAGT-IIIc from Obu et al. (2019) had the strongest linear relationship; however, all MAGTs performed similarly. MAGT-II had a positive bias, while the TTOP MAGTs (III) all had negative biases, the least of which is based on soil moisture estimates from GLDAS. The dark purple to yellow gradient in each plot represents a kernel density distribution based on the total number of points. (For interpretation of the references to colour in this figure legend, the reader is referred to the web version of this article.)

comparable estimates between the temperature at the DZAA and surface MAGT (Luo et al., 2018a). On the other hand, the wet bias of the ERA5-L soil moisture averages is evident in the colder temperatures of the modeled TTOP (IIIb). The GLDAS-based TTOP performed better across all metrics, and the results are instructive for demonstrating the sensitivity of ground temperatures to soil moisture conditions. Nevertheless, the performance of all MAGTs were comparable, with all biases and RMSEs less than an absolute value of 1 °C when validated against borehole measurements, apart from MAGT-IIIb (ERA5-L) and IIIc (Obu et al., 2019), whose estimates were less accurate.

Table 7 shows that the gap-filled MAGT (Ia) omitting the influence of snow cover or soil moisture conditions performed the best, relative to the modeled MAGTs of this study. Although these metrics may largely be caused by the inherent errors of the applied snow depth and soil

Table 7
Validation of MAGTs (mean annual ground temperatures). The RSME and bias are in units of °C. The highest performing metrics are bolded, while the lowest are italicized.

	Seasonally Frozen Ground			Borehole			All Sites		
MAGT	r	RMSE	bias	r	RMSE	bias	r	RMSE	bias
Ia	0.773	**0.890**	**0.003**	0.560	0.680	0.462	0.812	**0.762**	0.225
II	0.743	1.927	0.844	0.519	0.963	0.791	0.801	1.378	0.818
IIIa (GLDAS)	0.726	2.271	−0.621	0.504	0.698	−0.306	0.786	1.556	−0.469
IIIb (ERA5-L)	0.690	*2.488*	−1.055	0.495	1.015	−0.770	0.767	*1.778*	−0.917
IIIc (Obu et al., 2019)	**0.783**	1.509	*−1.135*	*0.362*	*1.293*	*−1.121*	**0.821**	1.316	*−1.128*
IV (Ran et al., 2022)	*0.641*	1.779	−0.225	**0.670**	**0.563**	**0.020**	*0.728*	1.205	**−0.099**

moisture datasets, they also indicate the reliability of the remotely sensed surface temperature product. Because the MAGTs of this study were not fitted to any available *in situ* dataset, unlike the Ran et al. (2022) estimates, these results are encouraging, showing the practicality of remotely sensed MAGTs across locations in High Mountain Asia where no prior data is available. Accounting for the persistent cold bias

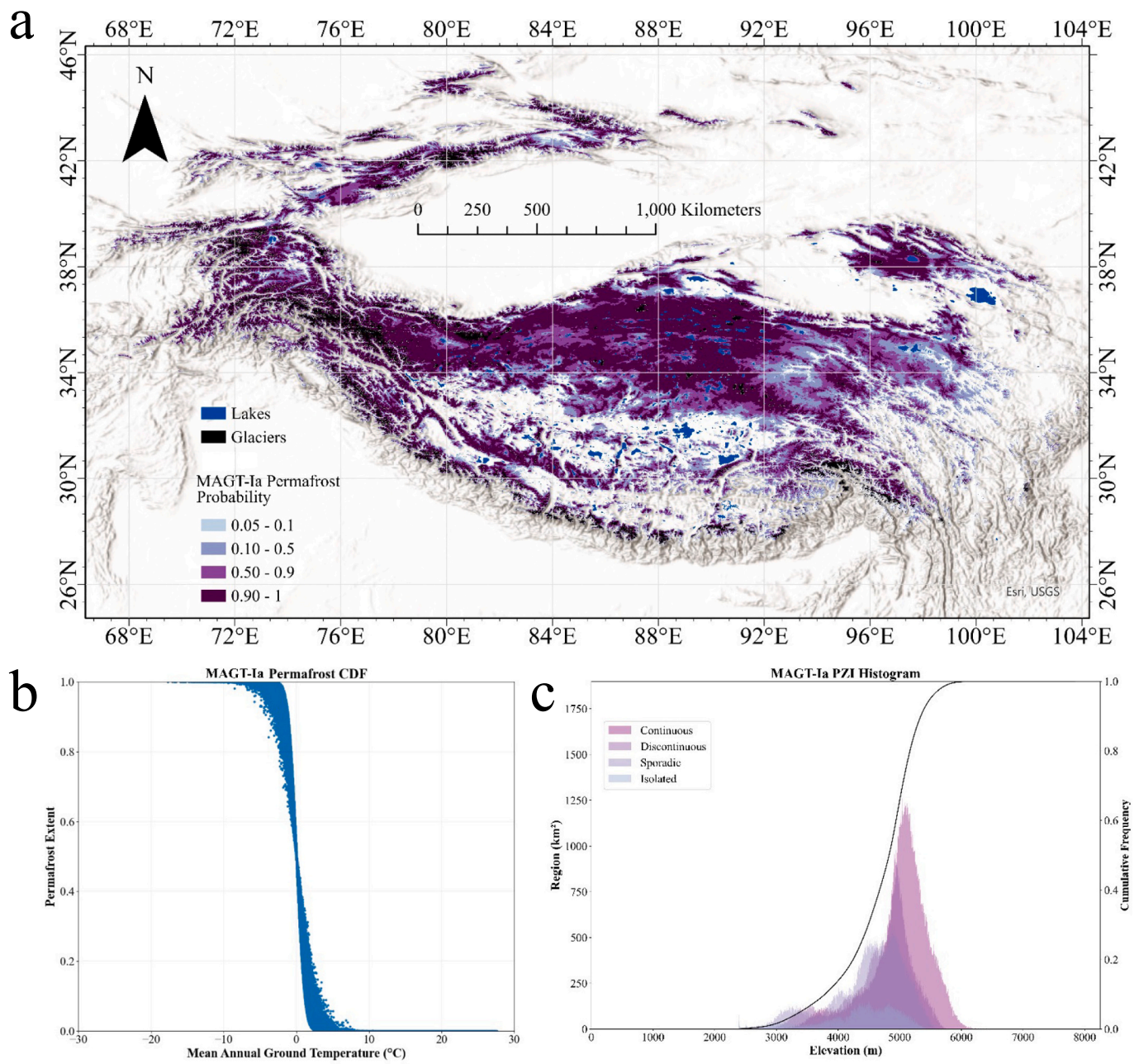

Fig. 7. a) Permafrost Zonation Index (PZI) calculated with MAGT-Ia (2003–2016) b) Cumulative distribution of the range of all permafrost extent probabilities associated with a modeled total variance of the MAGT (Eq. (8)). c) Histograms of the total permafrost region, as defined by the extent of the four permafrost zones using MAGT-Ia, against elevation.

in MAGT-IIIc from Obu et al. (2019) and the limitation of MAGT-IV (Ran et al., 2022) in data scarce mountain regions, the MAGTs based on the fusion of MODIS and AIRS temperature estimates demonstrate comparable, if not better, performance.

3.4. PZIs and estimated permafrost regions

The PZIs produced from this study exhibit similar spatial distributions as the other permafrost indices for HMA (Gruber, 2012; Obu et al., 2019; Ran et al., 2022). Fig. 7a is the categorized PZI map based on the MAGT-Ia, with most of the "continuous" (or alternatively, most likely, from 90 to 100%) permafrost concentrated around the Tibetan Plateau, Kunlun, Qilian, Gandise, Tien Shan, and east of the Karakoram. Eastern HMA exhibits decreasing permafrost extent, classified by lower probabilities. Fig. 7b shows the cumulative distribution of permafrost extent plotted against the MAGT-Ia, with the likelihood of permafrost presence approaching 5% (the assumed limit of permafrost zonation in this study) and below at about 2 °C. Fig. 7c is the histogram depicting the cumulative frequency of the permafrost region of HMA, distinguished by the four permafrost zones, against elevation. The clustering of permafrost between 3000 and 6000 m.a.s.l. suggests an optimal elevation range, below or above which permafrost is unlikely to develop or exist. Since direct solar radiation and aridity increases with higher elevations, this result agrees with previous works that suggest an elevation dependence for alpine permafrost in HMA (Marchenko et al., 2007; Gruber et al., 2017). Cold-arid climatologies as determined by precipitation patterns and soil moisture conditions, and minimal snow cover are likely to be the deciding factor for permafrost presence at these lower altitudes; for example, in the Tien Shan, whose permafrost regions are detected at lower elevation bands relative to other regions (Fig. 8). Additional histograms and CDFs of all PZIs are available in the supplementary text (Figs. S6 and S7).

Fig. 9 shows a comparison of permafrost presence as determined by regional area between the MAGT-Ia and the DZAA-based MAGT-IV from Ran et al. (2022) and the MAAT-based MAGT-Ib PZIs from Gruber (2012). Its comparison against the MAGT-IV PZI reveals a similar pattern in permafrost extent, in which the PZI based on the DZAA-targeted MAGT (IV) exhibits a similar geographic distribution to the surface retrievals solely based on remotely sensed data (Fig. 9a). However, its comparison with the MAGT-Ib PZI, which is based on an assumed offset between the MAAT and MAGT (Gruber, 2012), shows noticeable decreases across central and eastern HMA, but also a distinct increase in the Tien Shan and West of the Himalayas (Fig. 9b).

Fig. 10a shows the relative permafrost regional areas across all the mountain ranges of HMA. The PZIs from Gruber's MAAT-based MAGT (Ib) (Gruber, 2012) and TTOPs (III) from this study are comparable, while the permafrost extents predicted by MAGT-Ia, MAGT-II, MAGT-IV (Ran et al., 2022) and even the MAGT-IIIc PZI from Obu et al. (2019) are lower. However, the MAGT-Ia PZI does predict more permafrost across the northwestern mountain ranges. Fig. 10b shows the distribution of estimated permafrost regions according to the calculated PZIs of this study as well as the previously published PZIs. Regions with more persistent snow cover to the West have the least variability in relative permafrost extent. The greatest variability, relative to their total areas, exists for the Hengduan and Himalayas, with coefficients of variation (CV) of about 52% and 44%, respectively. All permafrost regional areas and CVs are presented in Table 8.

The calculated regional areas for the MAGT-Ia, MAGT-II, and MAGT-III PZIs (GLDAS [a] and ERA5-L [b]) result in about 1.50 million, 1.47 million, 1.93 million, and 2.15 million km^2 of permafrost cover, respectively. These totals vary as much as the estimates calculated with the TTOP MAGT-IIIc permafrost index by Obu et al. (2019) at about 1.56 million km^2 and the MAGT-Ib PZI by Gruber at about 1.95 million km^2 (Gruber, 2012). However, the total regional estimate based on the

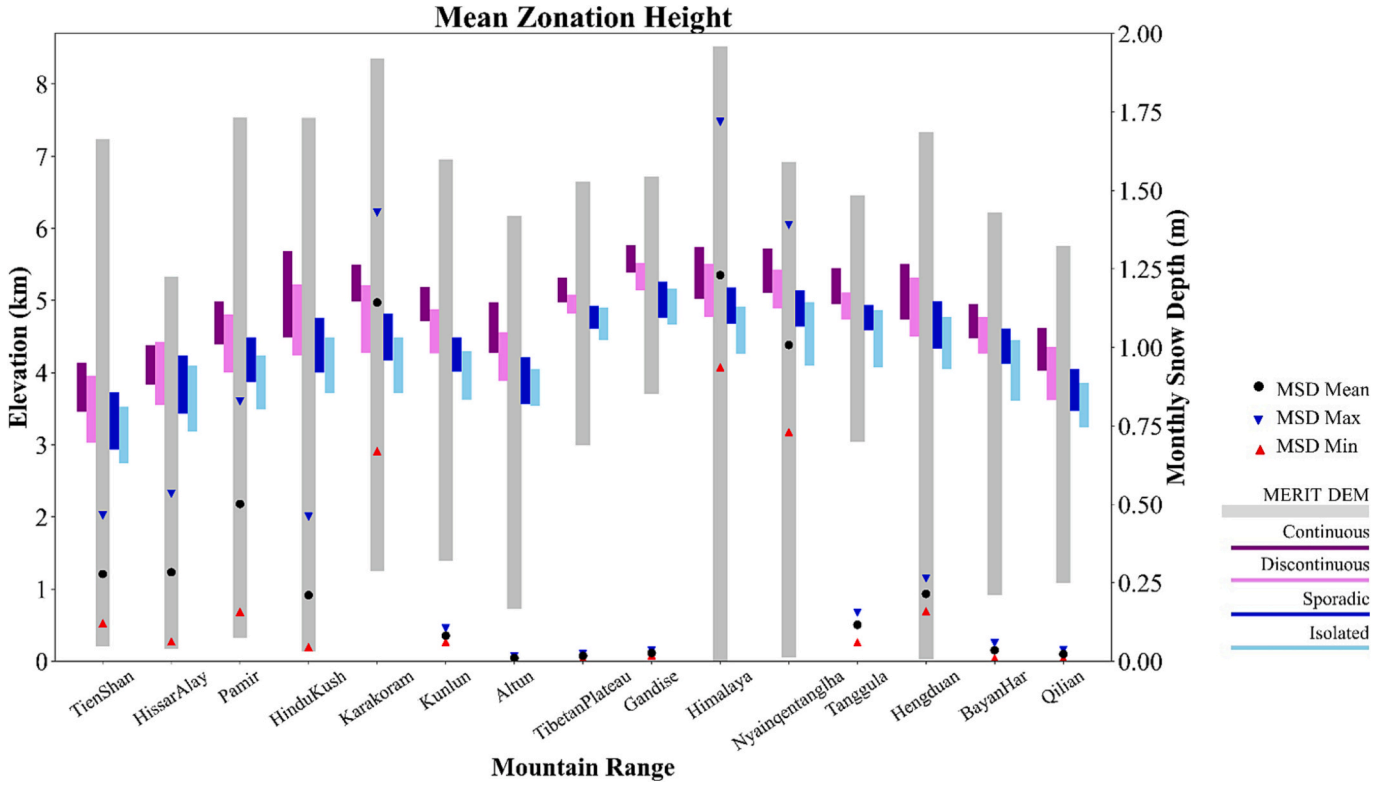

Fig. 8. The altitude range (maximum to minimum) of permafrost zonation across all calculated PZIs (permafrost zonation indices) are plotted for the mountain ranges of HMA (High Mountain Asia), from the northwest (left) to the northeast (right), alongside spatially averaged monthly snow depth means, maximums, and minimums for the 2003–2016 study period based on the HMA Snow Reanalysis dataset (Liu et al., 2021). The gray line in the center denotes the elevation range of each region.

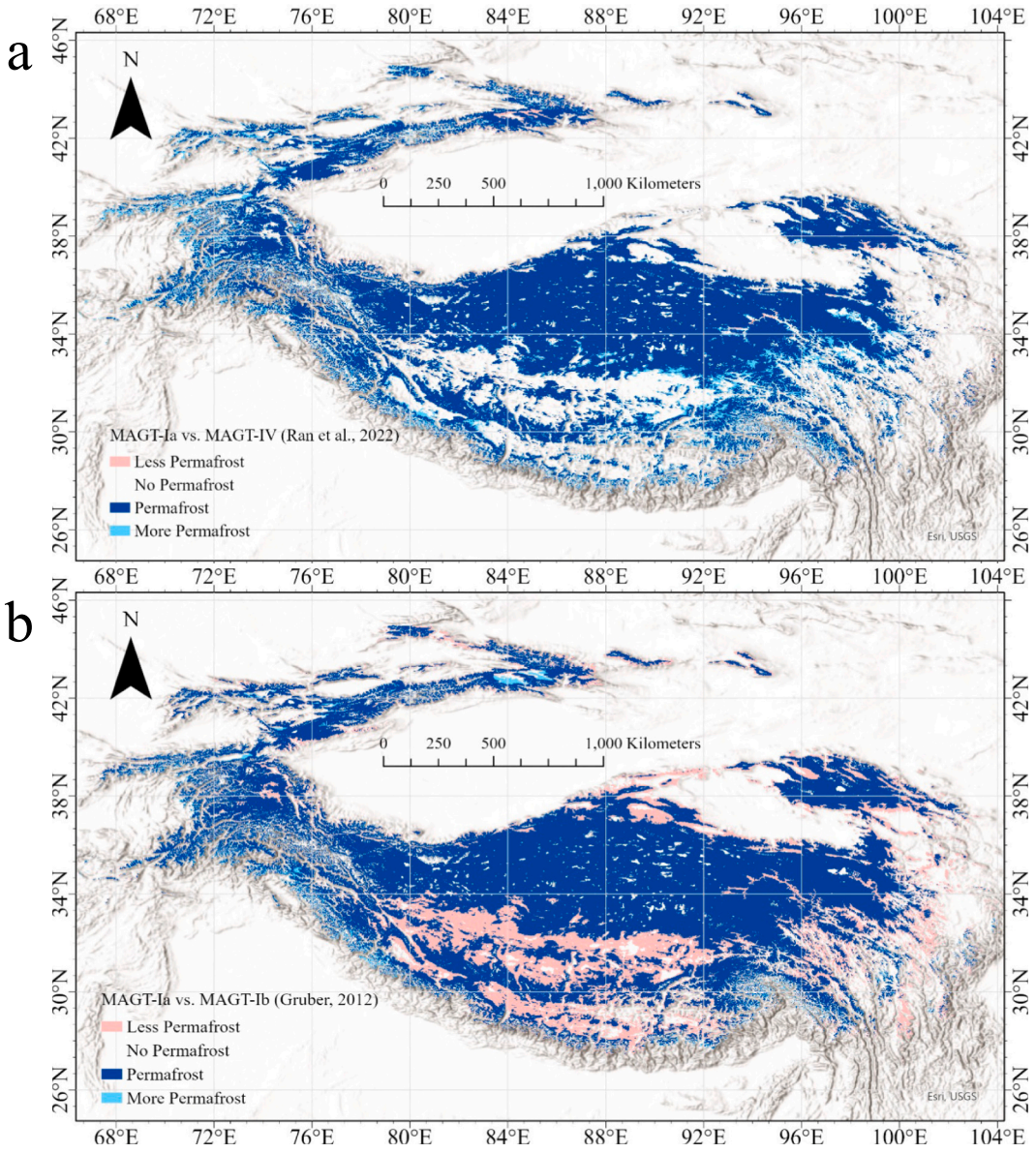

Fig. 9. The MAGT-Ia PZI (permafrost zonation index) without either the snow depth or thermal offset correction is compared with the PZIs derived from (a) the DZAA (depth of zero annual amplitude)-based MAGT-IV (Ran et al., 2022) and (b) MAGT-Ib (Gruber, 2012). Less permafrost was estimated across most of central and eastern High Mountain Asia between the MAGT-Ia and MAGT-Ib PZIs, while similar permafrost regional extents exist between MAGT-Ia and the MAGT-IV based estimates.

MAGT-IV by Ran et al. (2022) is comparatively lower, at about 1.28 million km^2. Table 9 shows the resulting confusion matrix of a pixel-to-pixel analysis, with percentages of total shared permafrost (or non-permafrost) regions. The MAGT-Ia PZI without additional offset corrections had the most agreement across the reviewed PZIs, agreeing with about 93–94% of the PZIs from Obu et al. (2019) and Ran et al. (2022). However, the MAGT-III PZI with GLDAS (a) soil moisture estimates had good agreement (93%) with the MAGT-Ib PZI from Gruber (2012).

4. Discussion

Our methodology implements a novel, robust approach for gap-filling MODIS-based land surface temperature estimates with the complementary skin surface temperature retrievals from AIRS onboard the Aqua satellite. The bias towards clear sky estimates in MODIS products is addressed with the AIRS' ability to rigorously determine temperatures below cloud cover and allows for sufficient filtering when assessing quality control for the MODIS retrievals, especially during the monsoon season, which frequently captures temperatures of the cloud surface. With some land surface temperature estimates approaching −10 °C in the middle of summer, even established gap-filling procedures are vulnerable to propagated errors and biases (Figs. 3 and S2; Table 6). Furthermore, our PZIs highlight the sensitivity of permafrost conditions to snow depth and soil moisture by using products that needed to be further assessed with respect to permafrost mapping. Although biased, as shown in the validations with available monthly *in situ* observations (Supplementary Figs. S3 and S4), the final PZI comparisons contextualize the practicality of incorporating modeled products. Without a more continuous set of data across the complex topography of HMA, these products suggest adequate performance when investigating the range of possible permafrost conditions and stability. Furthermore, the cross-comparisons emphasize the key idea that TTOP-based (MAGT-III) extents may overestimate permafrost presence. The snow depth corrected (MAGT-II) PZI, however, shows that only correcting the insulating layer

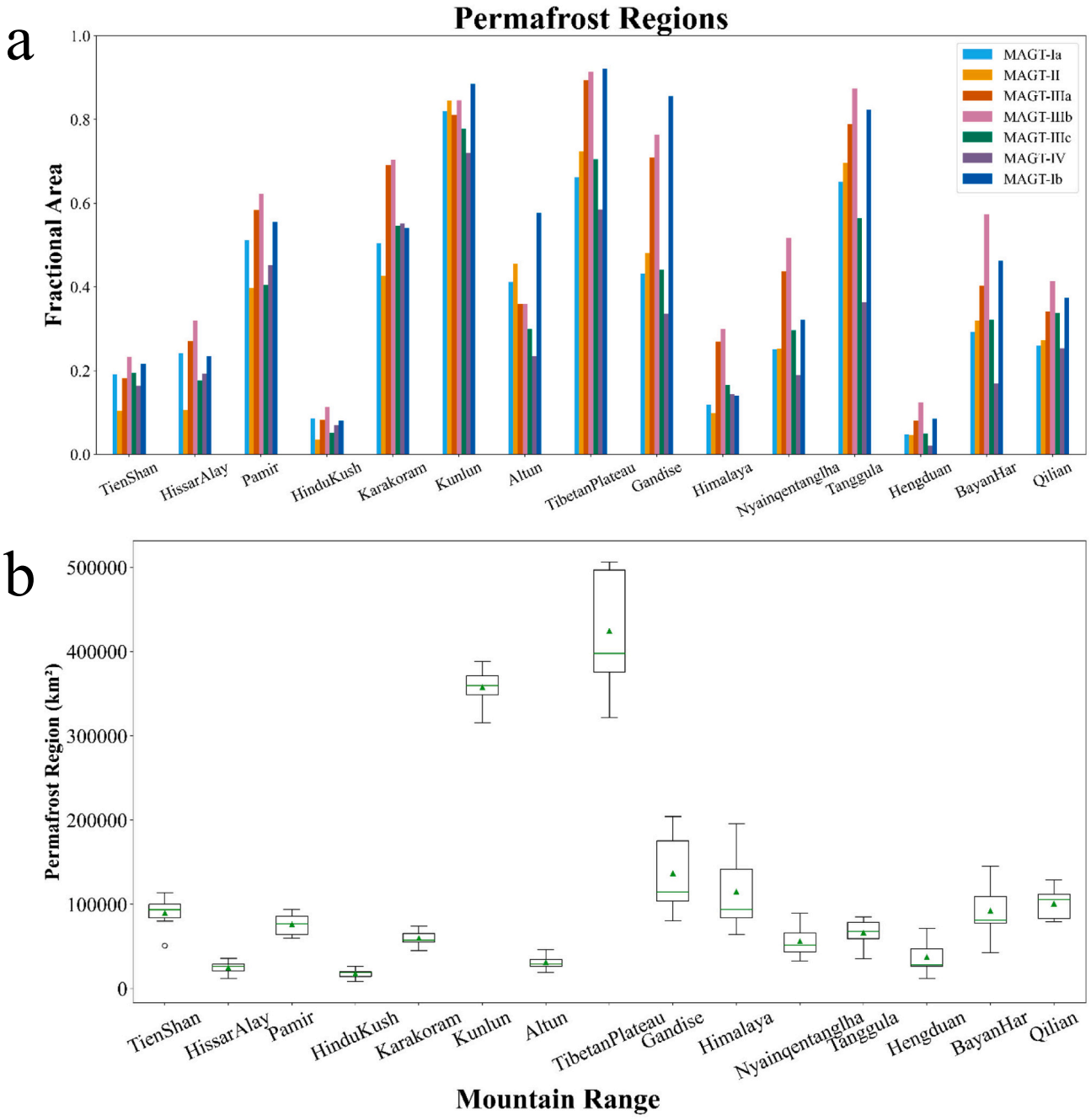

Fig. 10. a) Fractional permafrost regional areas for the different mountain ranges of the HMA (High Mountain Asia). Relatively, the largest permafrost areas were estimated with the TTOP-based MAGT-III models (and Gruber's MAAT-based MAGT-Ib PZI) and the least with either the MAGT-Ia without any offset calculations, the MAGT-II (only the nival factor), or MAGT-IV (Ran et al., 2022). b) A boxplot of the calculated permafrost regional areas was produced to compare the distribution of estimates across mountain ranges. The green triangle and line denote the mean and median, respectively. (For interpretation of the references to colour in this figure legend, the reader is referred to the web version of this article.)

of snow cover may lead to a warmer MAGT, underestimating total permafrost area. This is an important facet of this study, as the knowledge on permafrost extent is limited beyond the scope of the Tibetan Plateau, across the difficult-to-access regions of the northwest and southeast, which have different climatologies despite similar elevations. For example, although the Hengduan and Nyainqentanglha are in a wetter climate regime with higher MAGTs, more permafrost was consistently estimated with the TTOP-based PZIs because of a potential thermal offset due to the coexistence of water and ice and their contrasting thermal conductivities in the subsurface, allowing for permafrost even in regions where the surface MAGT is >0 °C. However, given the limited record of *in situ* ground temperature measurements with both snow depth and soil moisture data, this study's accuracy assessment may not fully represent the range of snow and moisture conditions across the entirety of High Mountain Asia. Furthermore, vegetation could still be an overlooked component, as MODIS LST products may retrieve temperatures above the canopy, which is denser to the east of the Tibetan Plateau (Cao et al., 2019a; Cao et al., 2019b). Therefore, the geographic differences between possible maximal and minimal permafrost coverage across a topography as complex as HMA

Table 8
A comparison of permafrost regions (in km^2) is presented across all PZIs (permafrost zonation indices) assessed in this study. The coefficient of variance (CV) is defined as the percentage of sample standard deviation divided by the mean.

Mountain Range	Ia	II	IIIa	IIIb	IIIc (Obu)	IV (Ran)	Ib (Gruber)	Average	St. Dev.	CV
Tien Shan	9.36×10^4	5.10×10^4	8.85×10^4	1.14×10^5	9.49×10^4	8.01×10^4	1.05×10^5	8.96×10^4	2.02×10^4	22.6%
Hissar Alay	2.73×10^4	1.20×10^4	3.05×10^4	3.60×10^4	1.99×10^4	2.17×10^4	2.66×10^4	2.49×10^4	7.79×10^3	31.3%
Pamir	7.72×10^4	6.02×10^4	8.82×10^4	9.41×10^4	6.11×10^4	6.82×10^4	8.40×10^4	7.61×10^4	1.34×10^4	17.6%
Hindu Kush	2.03×10^4	8.33×10^3	1.96×10^4	2.67×10^4	1.23×10^4	1.64×10^4	1.90×10^4	1.75×10^4	5.93×10^3	33.8%
Karakoram	5.34×10^4	4.50×10^4	7.29×10^4	7.43×10^4	5.77×10^4	5.83×10^4	5.71×10^4	5.98×10^4	1.05×10^4	17.5%
Kunlun	3.60×10^5	3.71×10^5	3.56×10^5	3.71×10^5	3.42×10^5	3.16×10^5	3.88×10^5	3.58×10^5	2.35×10^4	6.56%
Altun	3.31×10^4	3.67×10^4	2.90×10^4	2.90×10^4	2.42×10^4	1.90×10^4	4.65×10^4	3.11×10^4	8.93×10^3	28.7%
Tibetan Plateau	3.64×10^5	3.98×10^5	4.92×10^5	5.02×10^5	3.87×10^5	3.22×10^5	5.06×10^5	4.24×10^5	7.48×10^4	17.6%
Gandise	1.03×10^5	1.15×10^5	1.69×10^5	1.82×10^5	1.05×10^5	8.02×10^4	2.04×10^5	1.37×10^5	4.74×10^4	34.6%
Himalaya	7.70×10^4	6.44×10^4	1.76×10^5	1.96×10^5	1.08×10^5	9.38×10^4	9.12×10^4	1.15×10^5	5.04×10^4	43.8%
Nyainqentanglha	4.36×10^4	4.39×10^4	7.58×10^4	8.98×10^4	5.16×10^4	3.28×10^4	5.60×10^4	5.62×10^4	2.00×10^4	35.5%
Tanggula	6.36×10^4	6.81×10^4	7.70×10^4	8.54×10^4	5.52×10^4	3.56×10^4	8.04×10^4	6.65×10^4	1.71×10^4	25.7%
Hengduan	2.76×10^4	2.64×10^4	4.62×10^4	7.12×10^4	2.87×10^4	1.24×10^4	4.90×10^4	3.74×10^4	1.95×10^4	52.1%
Bayan Har	7.42×10^4	8.11×10^4	1.02×10^5	1.45×10^5	8.16×10^4	4.30×10^4	1.17×10^5	9.21×10^4	3.30×10^4	35.8%
Qilian	8.11×10^4	8.55×10^4	1.07×10^5	1.29×10^5	1.06×10^5	7.93×10^4	1.17×10^5	1.01×10^5	1.93×10^4	19.1%
TOTAL	1.50×10^6	1.47×10^6	1.93×10^6	2.15×10^6	1.54×10^6	1.28×10^6	1.95×10^6	1.69×10^6	3.19×10^5	18.9%

Table 9
A confusion matrix showing shared and un-shared permafrost (non-)regions between the permafrost indices. The values are all shown as percentages, with the greatest overlap bolded per row. The total common areas (Permafrost, **P**, and Non-Permafrost, **N**) are italicized in the corresponding column and row.

	Ia		II		IIIa (GLDAS)		IIIb (ERA5-L)		IIIc (Obu)		IV (Ran)	
	P	**N**	**P**	**N**	**P**	**N**	**P**	**N**	**P**	**N**	**P**	**N**
II	***94.8%***											
P	30.5	3.0										
N	2.2	62.3										
IIIa (GLDAS)	*88.0%*		*88.6%*									
P	32.3	0.5	32.5	0.0								
N	11.6	55.7	11.4	56.1								
IIIb (ERA5-L)	*83.9%*		*83.7%*		***94.9%***							
P	32.8	0.0	32.5	0.0	43.8	0.1						
N	16.1	51.1	16.3	51.2	5.0	51.1						
IIIc (Obu et al., 2019)	***92.8%***		*92.6%*		*89.2%*		*85.8%*					
P	30.3	2.6	30.0	2.5	34.0	9.9	34.8	14.0				
N	4.7	62.5	4.9	62.6	0.9	55.2	0.1	51.0				
IV (Ran et al., 2022)	***93.7%***		*91.6%*		*84.4%*		*80.1%*		*91.3%*			
P	27.8	5.0	26.6	5.9	28.7	15.2	29.0	19.8	27.6	7.3		
N	1.3	65.9	2.5	65.0	0.4	55.7	0.0	51.1	1.4	63.7		
Ib (Gruber, 2012)	*87.8%*		*88.2%*		***93.3%***		*91.0%*		*88.0%*		*84.4%*	
P	32.4	1.1	32.2	0.5	40.6	15.2	42.0	7.4	33.5	2.0	28.8	0.8
N	11.1	55.4	11.3	56.0	0.4	55.7	1.6	49.0	10.0	54.5	14.7	55.6

are informative for highlighting the opposing influences surface variables have on ground temperatures. Because snow depth and soil moisture in mountain environments are historically difficult to estimate, their associated PZIs are presented to demonstrate sensitivity to these variables. Fortunately, current avenues of research based on active radar retrievals and a growing record of observations (both *in situ* and remotely sensed) appear to be promising (Babaeian et al., 2019; Lievens et al., 2019).

For the Tien Shan and its neighboring mountains, similar permafrost regional areas were estimated by this study's and previous PZIs. This shows that available methods for permafrost mapping are reaching similar regional estimates (Fig. 10). On the other hand, an unrecognized bias may exist, which the snow-corrected MAGT-II PZI suggests. When only accounting for snow cover, much less permafrost is estimated due to the region's climatology, in which the westerlies contribute to significant snow accumulations (Li et al., 2020a, 2020b). Of the estimated continuous permafrost subregions, the Tien Shan's relatively lower elevation threshold is an important but confounding component (Fig. 10). Another observation is the discrepancy of permafrost extent for two basin-like features in the Tien Shan. MAGT-Ia, III, IV PZIs estimate high probabilities; however, both MAGT-II and MAGT-Ib (Gruber, 2012) PZIs have conflicting conclusions with lower permafrost probabilities. MAGT-Ia appears to reveal a long-term temperature inversion in such locations. For example, the intercomparison of PZIs for the Tibetan Plateau by Cao et al. (2019b) determined that Gruber (2012) may underestimate permafrost in valleys because cold air pooling is ignored.

With respect to the MAGT validations in Fig. 6 and Table 7, all MAGTs were similar in performance when assessed against the temperatures at the ground surface or active layer depths, with the MAGT-Ia of this study being the most robust. However, when validated against the borehole measurements, MAGT-II exhibited a warm bias, while the MAGT-III had cold biases. TTOP estimates from Obu et al. (2019) performed with the lowest accuracy (Table 7). In fact, Romanovsky and Osterkamp (2000) have noted that soils containing large amounts of unfrozen water exhibit decreased thermal offsets, which the TTOP approach may overestimate in discontinuous permafrost (Smith and Riseborough, 2002). This observation, along with the wet bias in available gridded soil moisture datasets, confirms these comparisons.

The variation between the different estimates is largely due to differences in the representation of snowpack, soil moisture and vegetation influence, and exhibits systematic regional trends (Table 8; Figs. 8 and 10). The CV (7–29%) is lowest in the central region (Altun, Kunlun and interior Tibetan Plateau), where snow cover is minimal year-round. In the north-western regions (Tien Shan, Hissar Alay, Pamir, Hindu Kush and Karakoram), where the snow cover is more persistent but variable than in the central region due to the influence of the westerlies, the CV is moderately low (18–31%). The CV is marginally higher (19–36%) in the Qilian, Tanggula and Bayan Har regions in the east, where there is greater heterogeneity in soil moisture and vegetation, in addition to the influence of snow. The CV is highest (26–52%) in the south (Nyainqentanglha, Hengduan, Himalayas, Gandise), where the significant influence of both snowpack and vegetation canopy is further complicated by warming trends (Table 4).

A surprising result is the robust performance of the MAGT-Ia estimate alone against the borehole temperatures. Despite a correlation coefficient of 0.56 and an RMSE of 0.68, it had the next best metrics of the group, behind only Ran et al. (2022), whose MAGTs were fitted to *in situ* measurements primarily recorded at the DZAA. This suggests a relationship between the MAGT on the land surface (Ia) and the MAGT at the DZAA which could be further monitored by satellite-based surface temperature products alone. In fact, a study by Luo et al. (2018a) reaches a related conclusion that minimal thermal offset exists between the MAGT within the active layer and DZAA MAGT in warm-dry permafrost, which could allow for accurate permafrost mapping with just the MAGT alone at a depth of 0-5 cm, after accounting for air temperature offsets (Luo et al., 2018a). Based on their comparison of the TTOP and DZAA MAGTs to the surface MAGTs in the headwaters of the Yangtze and Yellow Rivers by the Bayan Har region, they suggest that thermal conductivities of thawed and frozen ground do not need to be known for such permafrost layers. Given the nature of mountain permafrost, the distinction between DZAA and TTOP MAGT may be less important, especially in arid environments. However, neglecting the thermal influence of surface variables in ground temperature simulations forced with only *in situ* air or land surface temperature has also been documented to lead to cold biases in the MAGT by as much as 3 °C at depth in the same region (Luo et al., 2018b).

This implication must be contextualized in the era of anthropogenic climate change. Some regions are experiencing a statistically significant warming trend (*e.g.*, the Hengduan and Nyainqentanglha) as determined by preliminary results for non-stationarity in Table 4. Because ground temperatures lag air temperatures at different frequencies based on depth, it may be possible for the remotely sensed surface temperatures to erroneously infer warmer MAGTs. However, the study by Biskaborn et al. (2019) did reveal that permafrost in warmer thermal regimes experiences warming more slowly than their northern latitude counterparts. A more comprehensive study that compares historical and modern surface temperatures for HMA is necessary to better characterize the uncertainty associated with warming at depth. For example, one caveat of this study's comparisons against Gruber's MAGT-Ib PZI is that their MAGT was based on the MAAT of an older (and therefore presumably colder) period from 1961 to 1990, muddling the permafrost extent comparisons with a more recent period, from 2003 to 2016.

Another uncertainty associated with the comparisons is regarding the boundary between glaciated and non-glaciated regions. As permafrost tends to form in more arid climates, glaciers are the norm in humid regions like the Eastern Himalayas, which is indeed experiencing drastic ice loss due to warming air temperatures (Lee et al., 2021; Shean et al., 2020). However, the transition from permafrost to glacier is unclear at a resolution of 1 km, and the consequences of meltwater from retreating glaciers would impact subsurface temperatures, not unlike the relationship between the permafrost table and thermokarst lakes. Investigating the interaction between glacial melt and permafrost formation is therefore required to better understand the true probability of permafrost occurrence in such areas (Gruber and Haeberli, 2009; Waller et al., 2012; Etzelmüller, 2013).

Finally, a comment must be made regarding permafrost zonation. Although this study used the commonly used terminology of "continuous," "discontinuous", "sporadic", and "isolated" permafrost to categorize and compare the calculated permafrost extents, the approaches Ran et al. (2021, 2022) incorporated in their methods, by either hydrothermal zonation or stability type, offer important context. Given the heterogeneity in climate, topography, surface area, and solar radiation at high altitude, most of the permafrost in such areas range from "isolated" to "discontinuous," as mapped by Brown et al. (1997). By categorizing permafrost regimes in terms of climate and stability in addition to areal extent, a more nuanced discussion of mountain permafrost is possible (Ran et al., 2021).

5. Conclusions

This study produced a set of permafrost indices for HMA using monthly averages and a novel gap-filling procedure that leverages the availability of accurate remotely sensed observations onboard the Terra and Aqua satellites with the most up-to-date datasets. Though biased in validation, the modeled snow depth and soil moisture estimates demonstrated the influence of subsurface components on ground temperature variants, as shown through the sampled transect and *in situ* comparisons, highlighting that modeled temperatures at different depths must be investigated with nuance for delineating permafrost extent and potentially, stability. Building upon the work of previous studies, this research methodology emphasizes the importance of contextualizing MAGT validations at different depths for permafrost zonation.

The total permafrost extent for HMA as calculated with each index are 1.50 million (MAGT-Ia), 1.47 million (MAGT-II), 1.93 million (MAGT-IIIa [GLDAS]), 2.15 million (MAGT-IIIb [ERA5-L]), 1.54 million (MAGT-IIIc [Obu et al., 2019]), 1.28 million (MAGT-IV [Ran et al., 2022]), and 1.95 million (MAGT-Ib [Gruber, 2012]) km^2. On average, approximately 1.69 ($\pm$ 0.32) million km^2 of land in HMA is underlain with permafrost. The density of mountain permafrost is concentrated within a 4 to 6 km elevation band, with permafrost predicted to exist at an even lower limit of about 2.5 km in the Tien Shan. Geographically, the greatest discrepancy in permafrost regional estimates was to the south or east of the Tibetan Plateau, with the highest coefficients of variation (CVs) in the Hengduan (52%), Himalayas (44%), Bayan Har (36%), and Gandise (36%). Permafrost regions with the most agreement and lowest CVs were the Kunlun Mountains (7%), Pamirs (18%) and interior Tibetan Plateau (18%).

The findings based on our MODIS-AIRS gap-filled dataset agree well with the trained MAGT-IV estimates of Ran et al. (2022) and have shown that this method is a promising option for retrieving ground surface temperatures in data sparse, topographically complex areas such as HMA, improving upon even the most recent gap-filled MODIS LST product from Zhang et al. (2022). The new estimates for permafrost extent in HMA offers an increased level of confidence in the ability of remotely sensed products to monitor permafrost regimes, but not without the context of climate non-stationarity and microclimate factors finer than a 1 km scale. Therefore, we recommend the continued utilization of MODIS (MOD11/MYD11) and AIRS surface temperature products in the absence of more extensive data records.

Code availability

Algorithms for validations, gap-filling MODIS with AIRS temperature products, and calculating MAGT, PZIs, thermal conductivities, and snow depth corrections will be made available on the corresponding author's GitHub account.

Funding

This paper is based upon work supported by funding from the NASA HiMAT grant NASA Award Number 80NSSC20K1335 (NASA Program Manager Dr. Jared Entin): Improved Assessments of Permafrost and seasonally frozen ground in High Mountain Asia by Integrating Satellite Observations with Physics-Based Models and *In-Situ* Observations, as well as the National Science Foundation Research Traineeship (NRT) program under Grant No.1829004, the NSF Graduate Research Fellowship under Grant No.1842490, and Dean's Scholar Fellowship from the University of Virginia.

CRediT authorship contribution statement

Kyung Y. Kim: Writing – review & editing, Writing – original draft, Visualization, Validation, Software, Methodology, Investigation, Formal analysis, Data curation. **Ryan Haagenson:** Software. **Prakrut Kansara:** Software. **Harihar Rajaram:** Writing – review & editing, Supervision, Funding acquisition, Conceptualization. **Venkataraman Lakshmi:** Writing – review & editing, Supervision, Funding acquisition, Conceptualization.

Declaration of competing interest

The authors declare that they have no known competing financial interests or personal relationships that could have appeared to influence the work reported in this paper.

Data availability

The PZIs, MAGTs, gap-filled monthly MODIS-AIRS ground surface temperature estimates, and boundaries of the HMA mountain regions will be made available as a part of NASA HiMAT (https://himat.org/) by the corresponding author. Data supporting the conclusions of this study are properly cited and publicly available.

Acknowledgements

The authors would like to thank Johns Hopkins University, the University of Virginia, the data management team at NSIDC and LP DAAC for helping with data troubleshooting, all team members at NASA/HiMAT for open communication and advice, and the reviewers for their important feedback and suggestions during the revision process.

Appendix A. Supplementary data

Supplementary data to this article can be found online at https://doi.org/10.1016/j.rse.2024.114075.

References

Aalto, J., Karjalainen, O., Hjort, J., Luoto, M., 2018. Statistical forecasting of current and future Circum-Arctic ground temperatures and active layer thickness. Geophys. Res. Lett. 45, 4889–4898. https://doi.org/10.1029/2018GL078007.

Adolph, A.C., Albert, M.R., Hall, D.K., 2018. Near-surface temperature inversion during summer at summit, Greenland, and its relation to MODIS-derived surface temperatures. Cryosphere 12, 907–920. https://doi.org/10.5194/tc-12-907-2018.

Babaeian, E., Sadeghi, M., Jones, S.B., Montzka, C., Vereecken, H., Tuller, M., 2019. Ground, proximal, and satellite remote sensing of soil moisture. Rev. Geophys. 57, 530–616. https://doi.org/10.1029/2018RG000618.

Beaudoing, H., Rodell, M., 2020. GES DISC Dataset: GLDAS Noah Land Surface Model L4 monthly 0.25 x 0.25 degree V2.1 (GLDAS_NOAH025_M 2.1). URL. https://disc.gsfc.nasa.gov/datasets/GLDAS_NOAH025_M_2.1/summary (accessed 8.21.21).

Biskaborn, B.K., Smith, S.L., Noetzli, J., Matthes, H., Vieira, G., Streletskiy, D.A., Schoeneich, P., Romanovsky, V.E., Lewkowicz, A.G., Abramov, A., Allard, M., Boike, J., Cable, W.L., Christiansen, H.H., Delaloye, R., Diekmann, B., Drozdov, D., Etzelmüller, B., Grosse, G., Guglielmin, M., Ingeman-Nielsen, T., Isaksen, K., Ishikawa, M., Johansson, M., Johannsson, H., Joo, A., Kaverin, D., Kholodov, A., Konstantinov, P., Kröger, T., Lambiel, C., Lanckman, J.-P., Luo, D., Malkova, G., Meiklejohn, I., Moskalenko, N., Oliva, M., Phillips, M., Ramos, M., Sannel, A.B.K., Sergeev, D., Seybold, C., Skryabin, P., Vasiliev, A., Wu, Q., Yoshikawa, K., Zheleznyak, M., Lantuit, H., 2019. Permafrost is warming at a global scale. Nat. Commun. 10, 264. https://doi.org/10.1038/s41467-018-08240-4.

Bolch, T., Kulkarni, A., Kääb, A., Huggel, C., Paul, F., Cogley, J.G., Frey, H., Kargel, J.S., Fujita, K., Scheel, M., Bajracharya, S., Stoffel, M., 2012. The state and fate of Himalayan glaciers. Science 336, 310–314. https://doi.org/10.1126/science.1215828.

Bolch, T., Shea, J.M., Liu, S., Azam, F.M., Gao, Y., Gruber, S., Immerzeel, W.W., Kulkarni, A., Li, H., Tahir, A.A., Zhang, G., Zhang, Y., 2019. Status and change of the cryosphere in the extended Hindu Kush Himalaya region. In: Wester, P., Mishra, A., Mukherji, A., Shrestha, A.B. (Eds.), The Hindu Kush Himalaya Assessment: Mountains, Climate Change, Sustainability and People. Springer International Publishing, Cham, pp. 209–255. https://doi.org/10.1007/978-3-319-92288-1_7.

Boyd, D.W., 1976. Normal freezing and thawing degree-days from normal monthly temperatures. Can. Geotech. J. 13, 176–180. https://doi.org/10.1139/t76-018.

Brown, J., Ferrians Jr., O.J., Heginbottom, J.A., Melnikov, E.S., 1997. Circum-Arctic map of permafrost and ground-ice conditions. Circum-Pacific Map. https://doi.org/10.3133/cp45.

Cao, B., Zhang, T., Wu, Q., Sheng, Y., Zhao, L., Zou, D., 2019a. Permafrost zonation index map and statistics over the Qinghai–Tibet Plateau based on field evidence. Permafr. Periglac. Process. 30, 178–194. https://doi.org/10.1002/ppp.2006.

Cao, B., Zhang, T., Wu, Q., Sheng, Y., Zhao, L., Zou, D., 2019b. Brief communication: Evaluation and inter-comparisons of Qinghai–Tibet Plateau permafrost maps based on a new inventory of field evidence. Cryosphere 13, 511–519. https://doi.org/10.5194/tc-13-511-2019.

Che, T., Li, X., Liu, S., Li, H., Xu, Z., Tan, J., Zhang, Y., Ren, Z., Xiao, L., Deng, J., Jin, R., Ma, M., Wang, J., Yang, X., 2019. Integrated hydrometeorological, snow and frozen-ground observations in the alpine region of the Heihe River basin, China. Earth Syst. Sci. Data 11, 1483–1499. https://doi.org/10.5194/essd-11-1483-2019.

Christensen, T.R., Johansson, T., Åkerman, H.J., Mastepanov, M., Malmer, N., Friborg, T., Crill, P., Svensson, B.H., 2004. Thawing sub-arctic permafrost: effects on vegetation and methane emissions. Geophys. Res. Lett. 31 https://doi.org/10.1029/2003GL018680.

Collados-Lara, A.-J., Fassnacht, S.R., Pulido-Velazquez, D., Pfohl, A.K.D., Morán-Tejeda, E., Venable, N.B.H., Pardo-Igúzquiza, E., Puntenney-Desmond, K., 2021. Intra-day variability of temperature and its near-surface gradient with elevation over mountainous terrain: comparing MODIS land surface temperature data with coarse and fine scale near-surface measurements. Int. J. Climatol. 41, E1435–E1449. https://doi.org/10.1002/joc.6778.

Dente, L., Su, Z., Wen, J., 2012. Validation of smos soil moisture products over the Maqu and Twente regions. Sensors 12 (8), 9965–9986. https://doi.org/10.3390/s120809965.

Dorigo, W., Himmelbauer, I., Aberer, D., Schremmer, L., Petrakovic, I., Zappa, L., Preimesberger, W., Xaver, A., Annor, F., Ardö, J., Baldocchi, D., Bitelli, M., Blöschl, G., Bogena, H., Brocca, L., Calvet, J.-C., Camarero, J.J., Capello, G., Choi, M., Cosh, M.C., van de Giesen, N., Hajdu, I., Ikonen, J., Jensen, K.H., Kanniah, K.D., de Kat, I., Kirchengast, G., Kumar Rai, P., Kyrouac, J., Larson, K., Liu, S., Loew, A., Moghaddam, M., Martínez Fernández, J., Mattar Bader, C., Morbidelli, R., Musial, J.P., Osenga, E., Palecki, M.A., Pellarin, T., Petropoulos, G.P., Pfeil, I., Powers, J., Robock, A., Rüdiger, C., Rummel, U., Strobel, M., Su, Z., Sullivan, R., Tagesson, T., Varlagin, A., Vreugdenhil, M., Walker, J., Wen, J., Wenger, F., Wigneron, J.P., Woods, M., Yang, K., Zeng, Y., Zhang, X., Zreda, M., Dietrich, S., Gruber, A., van Oevelen, P., Wagner, W., Scipal, K., Drusch, M., Sabia, R., 2021. The international soil moisture network: serving earth system science for over a decade. Hydrol. Earth Syst. Sci. 25, 5749–5804. https://doi.org/10.5194/hess-25-5749-2021.

Dutra, E., Muñoz-Sabater, J., Boussetta, S., Komori, T., Hirahara, S., Balsamo, G., 2020. Environmental lapse rate for high-resolution land surface downscaling: an application to ERA5. Earth and Space Sci. 7 https://doi.org/10.1029/2019EA000984 e2019EA000984.

Etzelmüller, B., 2013. Recent advances in mountain permafrost research. Permafr. Periglac. Process. 24, 99–107. https://doi.org/10.1002/ppp.1772.

Fiddes, J., Gruber, S., 2014. TopoSCALE v.1.0: downscaling gridded climate data in complex terrain. Geosci. Model Dev. 7, 387–405. https://doi.org/10.5194/gmd-7-387-2014.

Furian, W., Loibl, D., Schneider, C., 2021. Future glacial lakes in High Mountain Asia: an inventory and assessment of hazard potential from surrounding slopes. J. Glaciol. 67, 653–670. https://doi.org/10.1017/jog.2021.18.

Gisnås, K., Etzelmüller, B., Farbrot, H., Schuler, T.V., Westermann, S., 2013. CryoGRID 1.0: Permafrost Distribution in Norway estimated by a Spatial Numerical Model. Periglac. Process. 24, 2–19. https://doi.org/10.1002/ppp.1765.

GLIMS and NSIDC, 2018. Global land ice measurements from space glacier database, v1. In: International GLIMS Community and the National Snow and Ice Data Center, Boulder. https://doi.org/10.7265/N5V98602.

Gruber, S., 2012. Derivation and analysis of a high-resolution estimate of global permafrost zonation. Cryosphere 6, 221–233. https://doi.org/10.5194/tc-6-221-2012.

Gruber, S., Haeberli, W., 2009. Mountain permafrost. In: Margesin, R. (Ed.), permafrost soils. Soil biology, 16. Springer, Berlin, Heidelberg. https://doi.org/10.1007/978-3-540-69371-0_3.

Gruber, S., Fleiner, R., Guegan, E., Panday, P., Schmid, M.-O., Stumm, D., Wester, P., Zhang, Y., Zhao, L., 2017. Review article: inferring permafrost and permafrost thaw in the mountains of the Hindu Kush Himalaya region. Cryosphere 11, 81–99. https://doi.org/10.5194/tc-11-81-2017.

Hachem, S., Allard, M., Duguay, C., 2009. Using the MODIS land surface temperature product for mapping permafrost: an application to northern Québec and Labrador, Canada. Permafr. Periglac. Process. 20, 407–416. https://doi.org/10.1002/ppp.672.
Hachem, S., Duguay, C.R., Allard, M., 2012. Comparison of MODIS-derived land surface temperatures with ground surface and air temperature measurements in continuous permafrost terrain. Cryosphere 6, 51–69. https://doi.org/10.5194/tc-6-51-2012.
Harris, R.I.D., 1992. Testing for unit roots using the augmented dickey-fuller test. Econ. Lett. 38, 381–386.
Harris, S.A., Brouchkov, A., Guodong, C., 2017. Geocryology: Characteristics and Use of Frozen Ground and Permafrost Landforms. CRC Press, London. https://doi.org/10.4324/9781315166988.
Hearty, T.J., Lee, J.N., Wu, D.L., Cullather, R., Blaisdell, J.M., Susskind, J., Nowicki, S.M. J., 2018. Intercomparison of surface temperatures from AIRS, MERRA, and MERRA-2, with NOAA and GC-net weather stations at summit, Greenland. J. Appl. Meteorol. Climatol. 57, 1231–1245. https://doi.org/10.1175/jamc-d-17-0216.1.
Hjort, J., Karjalainen, O., Aalto, J., Westermann, S., Romanovsky, V.E., Nelson, F.E., Etzelmüller, B., Luoto, M., 2018. Degrading permafrost puts Arctic infrastructure at risk by mid-century. Nat. Commun. 9, 5147. https://doi.org/10.1038/s41467-018-07557-4.
ICIMOD, 2021. GST (Ground Surface Temperature) Loggers. ICIMOD, Langtang Valley. 10.26066/RDS.1972553.
ICIMOD & NVE, 2012a. SnowAMP Upper. ICIMOD. 10.26066/RDS.1972504.
ICIMOD & NVE, 2012b. SnowAMP Lower. ICIMOD. 10.26066/RDS.1972502.
ICIMOD & NVE, 2012c. SnowAMP Middle. ICIMOD. 10.26066/RDS.1972503.
ICIMOD & NVE, 2012d. SnowAMP Ganja La. ICIMOD. 10.26066/RDS.1972505.
Immerzeel, W.W., van Beek, L.P.H., Bierkens, M.F.P., 2010. Climate change will affect the Asian water towers. Science 328, 1382–1385. https://doi.org/10.1126/science.1183188.
Kääb, A., Huggel, C., Fischer, L., Guex, S., Paul, F., Roer, I., Salzmann, N., Schlaefli, S., Schmutz, K., Schneider, D., Strozzi, T., Weidmann, Y., 2005. Remote sensing of glacier- and permafrost-related hazards in high mountains: an overview. Nat. Hazards Earth Syst. Sci. 5, 527–554. https://doi.org/10.5194/nhess-5-527-2005.
Karki, R., Hasson, S., Ul Schickhoff, U., Scholten, T., Böhner, J., Gerlitz, L., 2020. Near surface air temperature lapse rates over complex terrain: a WRF based analysis of controlling factors and processes for the Central Himalayas. Clim. Dyn. 54, 329–349. https://doi.org/10.1007/s00382-019-05003-9.
Kersten, M.S., 1949. Laboratory Research for the Determination of Thermal Properties of Soils. Arctic Construction and Frost Effects Laboratory, United States. https://hdl.handle.net/11681/6576.
Kwiatkowski, D., Phillips, P.C.B., Schmidt, P., Shin, Y., 1992. Testing the null hypothesis of stationarity against the alternative of a unit root: how sure are we that economic time series have a unit root? J. Econ. 54, 159–178. https://doi.org/10.1016/0304-4076(92)90104-Y.
Lee, E., Carrivick, J.L., Quincey, D.J., Cook, S.J., James, W.H.M., Brown, L.E., 2021. Accelerated mass loss of Himalayan glaciers since the little ice age. Sci. Rep. 11, 24284. https://doi.org/10.1038/s41598-021-03805-8.
Li, Z.-L., Tang, B.-H., Wu, H., Ren, H., Yan, G., Wan, Z., Trigo, I.F., Sobrino, J.A., 2013. Satellite-derived land surface temperature: current status and perspectives. Remote Sens. Environ. 131, 14–37. https://doi.org/10.1016/j.rse.2012.12.008.
Li, Y., Chen, Y., Li, Z., 2020a. Climate and topographic controls on snow phenology dynamics in the Tienshan Mountains, Central Asia. Atmos. Res. 236, 104813 https://doi.org/10.1016/j.atmosres.2019.104813.
Li, B., Chen, Y., Shi, X., 2020b. Does elevation dependent warming exist in high mountain Asia? Environ. Res. Lett. 15, 024012 https://doi.org/10.1088/1748-9326/ab6d7f.
Li, D., Lu, X., Walling, D.E., Zhang, T., Steiner, J.F., Wasson, R.J., Harrison, S., Nepal, S., Nie, Y., Immerzeel, W.W., Shugar, D.H., Koppes, M., Lane, S., Zeng, Z., Sun, X., Yegorov, A., Bolch, T., 2022. High Mountain Asia hydropower systems threatened by climate-driven landscape instability. Nat. Geosci. 15, 520–530. https://doi.org/10.1038/s41561-022-00953-y.
Lievens, H., Demuzere, M., Marshall, H.-P., Reichle, R.H., Brucker, L., Brangers, I., de Rosnay, P., Dumont, M., Girotto, M., Immerzeel, W.W., Jonas, T., Kim, E.J., Koch, I., Marty, C., Saloranta, T., Schöber, J., De Lannoy, G.J.M., 2019. Snow depth variability in the northern hemisphere mountains observed from space. Nat. Commun. 10, 4629. https://doi.org/10.1038/s41467-019-12566-y.
Liu, Y., Fang, Y., Margulis, S.A., 2021. Spatiotemporal distribution of seasonal snow water equivalent in High Mountain Asia from an 18-year Landsat–MODIS era snow reanalysis dataset. Cryosphere 15, 5261–5280. https://doi.org/10.5194/tc-15-5261-2021.
Liu, K., Song, C., Ke, L., Jiang, L., Pan, Y., Ma, R., 2019. Global open-access DEM performances in Earth's most rugged region High Mountain Asia: A multi-level assessment. Geomorphology 338, 16–26. https://doi.org/10.1016/j.geomorph.2019.04.012.
Lu, P., Han, J., Li, Z., Xu, R., Li, R., Hao, T., Qiao, G., 2020. Lake outburst accelerated permafrost degradation on Qinghai-Tibet plateau. Remote Sens. Environ. 249, 112011 https://doi.org/10.1016/j.rse.2020.112011.
Lunardini, V.J., 1981. Heat Transfer in Cold Climates, first ed. Van Nostrand Reinhold Co, New York.
Luo, D., Jin, H., Wu, Q., Bense, V.F., He, R., Ma, Q., Gao, S., Jin, X., Lü, L., 2018a. Thermal regime of warm-dry permafrost in relation to ground surface temperature in the source areas of the Yangtze and yellow rivers on the Qinghai-Tibet plateau, SW China. Sci. Total Environ. 618, 1033–1045. https://doi.org/10.1016/j.scitotenv.2017.09.083.
Luo, D., Jin, H., Marchenko, S.S., Romanovsky, V.E., 2018b. Difference between near-surface air, land surface and ground surface temperatures and their influences on the frozen ground on the Qinghai-Tibet plateau. Geoderma 312, 74–85. https://doi.org/10.1016/j.geoderma.2017.09.037.
Ma, Y., Hu, Z., Xie, Z., Ma, W., Wang, B., Chen, X., Li, M., Zhong, L., Sun, F., Gu, L., Han, C., Zhang, L., Liu, X., Ding, Z., Sun, G., Wang, S., Wang, Y., Wang, Z., 2020. A long-term (2005–2016) dataset of hourly integrated land–atmosphere interaction observations on the Tibetan plateau. Earth Syst. Sci. Data 12, 2937–2957. https://doi.org/10.5194/essd-12-2937-2020.
Marchenko, S.S., Gorbunov, A.P., Romanovsky, V.E., 2007. Permafrost warming in the Tien Shan Mountains, Central Asia. Global Planet. Change, Northern Eurasia Reg. Clim. Environ. Chan. 56, 311–327. https://doi.org/10.1016/j.gloplacha.2006.07.023.
Margulis, S.A., Liu, Y., Baldo, E., 2019. A joint Landsat- and MODIS-based reanalysis approach for Midlatitude montane seasonal snow characterization. Front. Earth Sci. 7, 272. https://doi.org/10.3389/feart.2019.00272.
Menne, M.J., Durre, I., Vose, R.S., Gleason, B.E., Houston, T.G., 2012. An overview of the global historical climatology network-daily database. J. Atmos. Ocean. Technol. 29, 897–910. https://doi.org/10.1175/JTECH-D-11-00103.1.
Metz, M., Andreo, V., Neteler, M., 2017. A new fully gap-free time series of land surface temperature from MODIS LST data. Remote Sens. 9, 1333. https://doi.org/10.3390/rs9121333.
Muñoz-Sabater, J., Dutra, E., Agustí-Panareda, A., Albergel, C., Arduini, G., Balsamo, G., Boussetta, S., Choulga, M., Harrigan, S., Hersbach, H., Martens, B., Miralles, D.G., Piles, M., Rodríguez-Fernández, N.J., Zsoter, E., Buontempo, C., Thépaut, J.-N., 2021. ERA5-land: a state-of-the-art global reanalysis dataset for land applications. Earth Syst. Sci. Data 13, 4349–4383. https://doi.org/10.5194/essd-13-4349-2021.
Mutiibwa, D., Strachan, S., Albright, T., 2015. Land surface temperature and surface air temperature in complex terrain. IEEE J. Select. Top. Appl. Earth Observat. Remote Sens. 8, 4762–4774. https://doi.org/10.1109/JSTARS.2015.2468594.
Noad, N.C., Bonnaventure, P.P., 2022. Surface temperature inversion characteristics in dissimilar valleys, Yukon Canada. Arctic Sci. 8, 1320–1339. https://doi.org/10.1139/as-2021-0048.
Obu, J., Westermann, S., Bartsch, A., Berdnikov, N., Christiansen, H.H., Dashtseren, A., Delaloye, R., Elberling, B., Etzelmüller, B., Kholodov, A., Khomutov, A., Kääb, A., Leibman, M.O., Lewkowicz, A.G., Panda, S.K., Romanovsky, V., Way, R.G., Westergaard-Nielsen, A., Wu, T., Yamkhin, J., Zou, D., 2019. Northern hemisphere permafrost map based on TTOP modelling for 2000–2016 at 1 km2 scale. Earth Sci. Rev. 193, 299–316. https://doi.org/10.1016/j.earscirev.2019.04.023.
Pepin, N., Bradley, R.S., Diaz, H.F., Baraer, M., Caceres, E.B., Forsythe, N., Fowler, H., Greenwood, G., Hashmi, M.Z., Liu, X.D., Miller, J.R., Ning, L., Ohmura, A., Palazzi, E., Rangwala, I., Schöner, W., Severskiy, I., Shahgedanova, M., Wang, M.B., Williamson, S.N., Yang, D.Q., Mountain Research Initiative EDW Working Group, 2015. Elevation-dependent warming in mountain regions of the world. Nat. Clim. Chang. 5, 424–430. https://doi.org/10.1038/nclimate2563.
Péwé, T.L., 1983. Alpine permafrost in the contiguous United States: a review. Arct. Alp. Res. 15, 145–156. https://doi.org/10.1080/00040851.1983.12004339.
Qin, Y., Wu, T., Zhao, L., Wu, X., Li, R., Xie, C., Pang, Q., Hu, G., Qiao, Y., Zhao, G., Liu, G., Zhu, X., Hao, J., 2017. Numerical modeling of the active layer thickness and permafrost thermal state across Qinghai-Tibetan plateau. J. Geophys. Res. Atmos. 122, 11,604–11,620. https://doi.org/10.1002/2017JD026858.
Ran, Y., Li, X., Cheng, G., Zhang, T., Wu, Q., Jin, H., Jin, R., 2012. Distribution of permafrost in China: an overview of existing permafrost maps. Permafr. Periglac. Process. 23, 322–333. https://doi.org/10.1002/ppp.1756.
Ran, Y., Li, X., Cheng, G., Nan, Z., Che, J., Sheng, Y., Wu, Q., Jin, H., Luo, D., Tang, Z., Wu, X., 2021. Mapping the permafrost stability on the Tibetan plateau for 2005–2015. Sci. China Earth Sci. 64, 62–79. https://doi.org/10.1007/s11430-020-9685-3.
Ran, Y., Li, X., Cheng, G., Che, J., Aalto, J., Karjalainen, O., Hjort, J., Luoto, M., Jin, H., Obu, J., Hori, M., Yu, Q., Chang, X., 2022. New high-resolution estimates of the permafrost thermal state and hydrothermal conditions over the northern hemisphere. Earth Syst. Sci. Data 14, 865–884. https://doi.org/10.5194/essd-14-865-2022.
Riggs, G.A., Hall, D.K., 2015. MODIS Snow Products Collection 6 User Guide.
Riseborough, D., Shiklomanov, N., Etzelmüller, B., Gruber, S., Marchenko, S., 2008. Recent advances in permafrost modeling. Permafr. Periglac. Process. 19, 137–156. https://doi.org/10.1002/ppp.615.
Rodell, M., Houser, P.R., Jambor, U., Gottschalck, J., Mitchell, K., Meng, C.-J., Arsenault, K., Cosgrove, B., Radakovich, J., Bosilovich, M., Entin, J.K., Walker, J.P., Lohmann, D., Toll, D., 2004. The global land data assimilation system. Bull. Am. Meteorol. Soc. 85, 381–394. https://doi.org/10.1175/BAMS-85-3-381.
Romanovsky, V.E., Osterkamp, T.E., 1995. Interannual variations of the thermal regime of the active layer and near-surface permafrost in northern Alaska. Permafr. Periglac. Process. 6, 313–335. https://doi.org/10.1002/ppp.3430060404.
Romanovsky, V.E., Osterkamp, T.E., 2000. Effects of unfrozen water on heat and mass transport processes in the active layer and permafrost. Permafr. Periglac. Process. 11, 219–239. https://doi.org/10.1002/1099-1530(200007/09)11:3<219::AID-PPP352>3.0.CO;2-7.
Schmid, M.-O., Baral, P., Gruber, S., Shahi, S., Shrestha, T., Stumm, D., Wester, P., 2015. Assessment of permafrost distribution maps in the Hindu Kush Himalayan region using rock glaciers mapped in Google earth. Cryosphere 9, 2089–2099. https://doi.org/10.5194/tc-9-2089-2015.
Schuur, E.A.G., McGuire, A.D., Schädel, C., Grosse, G., Harden, J.W., Hayes, D.J., Hugelius, G., Koven, C.D., Kuhry, P., Lawrence, D.M., Natali, S.M., Olefeldt, D., Romanovsky, V.E., Schaefer, K., Turetsky, M.R., Treat, C.C., Vonk, J.E., 2015. Climate change and the permafrost carbon feedback. Nature 520, 171–179. https://doi.org/10.1038/nature14338.

Shean, D.E., Bhushan, S., Montesano, P., Rounce, D.R., Arendt, A., Osmanoglu, B., 2020. A systematic, regional assessment of High Mountain Asia glacier mass balance. Front. Earth Sci. 7, 363. https://doi.org/10.3389/feart.2019.00363.
Smith, N., Barnet, C.D., 2023. Practical implications of CLIMCAPS cloud clearing and derived quality metrics. Earth and Space Sci. 10 https://doi.org/10.1029/2023EA002913 e2023EA002913.
Smith, M.W., Riseborough, D.W., 1996. Permafrost monitoring and detection of climate change. Permafr. Periglac. Process. 7, 301–309. https://doi.org/10.1002/(SICI)1099-1530(199610)7:4<301::AID-PPP231>3.0.CO;2-R.
Smith, M.W., Riseborough, D.W., 2002. Climate and the limits of permafrost: a zonal analysis. Permafr. Periglac. Process. 13, 1–15. https://doi.org/10.1002/ppp.410.
Smith, S.L., Riseborough, D.W., Bonnaventure, P.P., 2015. Eighteen year record of Forest fire effects on ground thermal regimes and permafrost in the Central Mackenzie Valley, NWT, Canada. Permafr. Periglac. Process. 26, 289–303. https://doi.org/10.1002/ppp.1849.
Smith, S.L., O'Neill, H.B., Isaksen, K., Noetzli, J., Romanovsky, V.E., 2022. The changing thermal state of permafrost. Nat. Rev. Earth Environ. 3, 10–23. https://doi.org/10.1038/s43017-021-00240-1.
Stigter, E.E., Wanders, N., Saloranta, T.M., Shea, J.M., Bierkens, M.F.P., Immerzeel, W. W., 2017. Assimilation of snow cover and snow depth into a snow model to estimate snow water equivalent and snowmelt runoff in a Himalayan catchment. Cryosphere 11, 1647–1664. https://doi.org/10.5194/tc-11-1647-2017.
Su, Z., Wen, J., Dente, L., van der Velde, R., Wang, L., Ma, Y., Yang, K., Hu, Z., 2011. The Tibetan plateau observatory of plateau scale soil moisture and soil temperature (Tibet-Obs) for quantifying uncertainties in coarse resolution satellite and model products. Hydrol. Earth Syst. Sci. 15, 2303–2316. https://doi.org/10.5194/hess-15-2303-2011.
Sun, Z., Ma, W., Zhang, S., Mu, Y., Yun, H., Wang, H., 2018. Characteristics of thawed interlayer and its effect on embankment settlement along the Qinghai-Tibet railway in permafrost regions. J. Mt. Sci. 15, 1090–1100. https://doi.org/10.1007/s11629-017-4643-1.
Sun, C., Chen, W., Shen, Y., 2022. Unraveling the distribution patterns of near-surface temperature lapse rates in the northwestern Kunlun Mountains. J. Mt. Sci. 19, 1168–1181. https://doi.org/10.1007/s11629-021-6983-0.
Susskind, J., Barnet, C.D., Blaisdell, J.M., 2003. Retrieval of atmospheric and surface parameters from AIRS/AMSU/HSB data in the presence of clouds. IEEE Trans. Geosci. Remote Sens. 41, 390–409. https://doi.org/10.1109/TGRS.2002.808236.
Susskind, J., Blaisdell, J.M., Iredell, L., Keita, F., 2011. Improved temperature sounding and quality control methodology using AIRS/AMSU data: the AIRS science team version 5 retrieval algorithm. IEEE Trans. Geosci. Remote Sens. 49, 883–907. https://doi.org/10.1109/TGRS.2010.2070508.
Susskind, J., Blaisdell, J.M., Iredell, L., 2014. Improved methodology for surface and atmospheric soundings, error estimates, and quality control procedures: the atmospheric infrared sounder science team version-6 retrieval algorithm. JARS 8, 084994. https://doi.org/10.1117/1.JRS.8.084994.
Turetsky, M.R., Abbott, B.W., Jones, M.C., Walter Anthony, K., Olefeldt, D., Schuur, E.A. G., Koven, C., McGuire, A.D., Grosse, G., Kuhry, P., Hugelius, G., Lawrence, D.M., Gibson, C., Sannel, A.B.K., 2019. Permafrost collapse is accelerating carbon release. Nature 569, 32–34. https://doi.org/10.1038/d41586-019-01313-4.
Vitasse, Y., Klein, G., Kirchner, J.W., Rebetez, M., 2017. Intensity, frequency and spatial configuration of winter temperature inversions in the closed La Brevine valley, Switzerland. Theor. Appl. Climatol. 130, 1073–1083. https://doi.org/10.1007/s00704-016-1944-1.
Waller, R.I., Murton, J.B., Kristensen, L., 2012. Glacier–permafrost interactions: processes, products and glaciological implications. Sediment. Geol. 255–256, 1–28. https://doi.org/10.1016/j.sedgeo.2012.02.005.
Wan, Z., 2014. New refinements and validation of the collection-6 MODIS land-surface temperature/emissivity product. Remote Sens. Environ. 140, 36–45. https://doi.org/10.1016/j.rse.2013.08.027.
Wan, Z., Dozier, J., 1996. A generalized split-window algorithm for retrieving land-surface temperature from space. IEEE Trans. Geosci. Remote Sens. 34, 892–905. https://doi.org/10.1109/36.508406.
Wan, W., Long, D., Hong, Y., Ma, Y., Yuan, Y., Xiao, P., Duan, H., Han, Z., Gu, X., 2016. A lake data set for the Tibetan plateau from the 1960s, 2005, and 2014. Sci. Data 3, 160039. https://doi.org/10.1038/sdata.2016.39.
Wang, B., French, H.M., 1995. Permafrost on the Tibet plateau, China. Quat. Sci. Rev. 14, 255–274. https://doi.org/10.1016/0277-3791(95)00006-B.
Wang, Q., Jin, H., Zhang, T., Cao, B., Peng, X., Wang, K., Xiao, X., Guo, H., Mu, C., Li, L., 2017. Hydro-thermal processes and thermal offsets of peat soils in the active layer in an alpine permafrost region, NE Qinghai-Tibet plateau. Glob. Planet. Chang. 156, 1–12. https://doi.org/10.1016/j.gloplacha.2017.07.011.
Wang, R., Zhu, Q., Ma, H., 2019. Changes in freezing and thawing indices over the source region of the Yellow River from 1980 to 2014. J. For. Res. 30, 257–268. https://doi.org/10.1007/s11676-017-0589-y.
Wani, J.M., Thayyen, R.J., Gruber, S., Ojha, C.S.P., Stumm, D., 2020. Single-year thermal regime and inferred permafrost occurrence in the upper Ganglass catchment of the cold-arid Himalaya, Ladakh, India. Sci. Total Environ. 703, 134631 https://doi.org/10.1016/j.scitotenv.2019.134631.
Westermann, S., Østby, T.I., Gisnås, K., Schuler, T.V., Etzelmüller, B., 2015. A ground temperature map of the North Atlantic permafrost region based on remote sensing and reanalysis data. Cryosphere 9, 1303–1319. https://doi.org/10.5194/tc-9-1303-2015.
Wu, T., Wang, Q., Zhao, L., Batkhishig, O., Watanabe, M., 2011. Observed trends in surface freezing/thawing index over the period 1987–2005 in Mongolia. Cold Reg. Sci. Technol. https://doi.org/10.1016/j.coldregions.2011.07.003. S0165232X11001364.
Wu, Q., Zhang, T., Liu, Y., 2012. Thermal state of the active layer and permafrost along the Qinghai-Xizang (Tibet) railway from 2006 to 2010. Cryosphere 6, 607–612. https://doi.org/10.5194/tc-6-607-2012.
Wu, T., Zhao, L., Li, R., Wang, Q., Xie, C., Pang, Q., 2013. Recent ground surface warming and its effects on permafrost on the Central Qinghai-Tibet plateau. Int. J. Climatol. 33, 920–930. https://doi.org/10.1002/joc.3479.
Wu, Q., Hou, Y., Yun, H., Liu, Y., 2015. Changes in active-layer thickness and near-surface permafrost between 2002 and 2012 in alpine ecosystems, Qinghai–Xizang (Tibet) Plateau, China. Glob. Planet. Chang. 124, 149–155. https://doi.org/10.1016/j.gloplacha.2014.09.002.
Wu, Z., Feng, H., He, H., Zhou, J., Zhang, Y., 2021. Evaluation of soil moisture climatology and anomaly components derived from ERA5-land and GLDAS-2.1 in China. Water Resour. Manag. 35, 629–643. https://doi.org/10.1007/s11269-020-02743-w.
Yamazaki, D., Ikeshima, D., Tawatari, R., Yamaguchi, T., O'Loughlin, F., Neal, J.C., Sampson, C.C., Kanae, S., Bates, P.D., 2017. A high-accuracy map of global terrain elevations. Geophys. Res. Lett. 44, 5844–5853. https://doi.org/10.1002/2017GL072874.
Yang, K., Qin, J., Zhao, L., Chen, Y.Y., Tang, W.J., Han, M.L., Lazhu, Z.Q., Chen, N., Lv, B. H., Ding, H., Wu, C.G. Lin, 2013. A multi-scale soil moisture and freeze-thaw monitoring network on the third pole. Bull. Am. Meteorol. Soc. https://doi.org/10.1175/BAMS-D-12-00203.1.
Zhang, T., 2005. Influence of the seasonal snow cover on the ground thermal regime: an overview. Rev. Geophys. 43 https://doi.org/10.1029/2004RG000157.
Zhang, T., Zhou, Y., Zhu, Z., Li, X., Asrar, G.R., 2022. A global seamless 1 km resolution daily land surface temperature dataset (2003–2020). Earth Syst. Sci. Data 14, 651–664. https://doi.org/10.5194/essd-14-651-2022.
Zhao, L., Zou, D., Hu, G., Wu, T., Du, E., Liu, G., Xiao, Y., Li, R., Pang, Q., Qiao, Y., Wu, X., Sun, Z., Xing, Z., Sheng, Y., Zhao, Y., Shi, J., Xie, C., Wang, L., Wang, C., Cheng, G., 2021. A synthesis dataset of permafrost thermal state for the Qinghai–Tibet (Xizang) Plateau, China. Earth Syst. Sci. Data 13, 4207–4218. https://doi.org/10.5194/essd-13-4207-2021.
Zheng, G., Yang, Y., Yang, D., Dafflon, B., Yi, Y., Zhang, S., Chen, D., Gao, B., Wang, T., Shi, R., Wu, Q., 2020. Remote sensing spatiotemporal patterns of frozen soil and the environmental controls over the Tibetan plateau during 2002–2016. Remote Sens. Environ. 247, 111927 https://doi.org/10.1016/j.rse.2020.111927.
Zou, D., Zhao, L., Sheng, Y., Chen, J., Hu, G., Wu, T., Wu, J., Xie, C., Wu, X., Pang, Q., Wang, W., Du, E., Li, W., Liu, G., Li, J., Qin, Y., Qiao, Y., Wang, Z., Shi, J., Cheng, G., 2017. A new map of permafrost distribution on the Tibetan plateau. Cryosphere 11, 2527–2542. https://doi.org/10.5194/tc-11-2527-2017.